CHALMERS
UNIVERSITY OF TECHNOLOGY

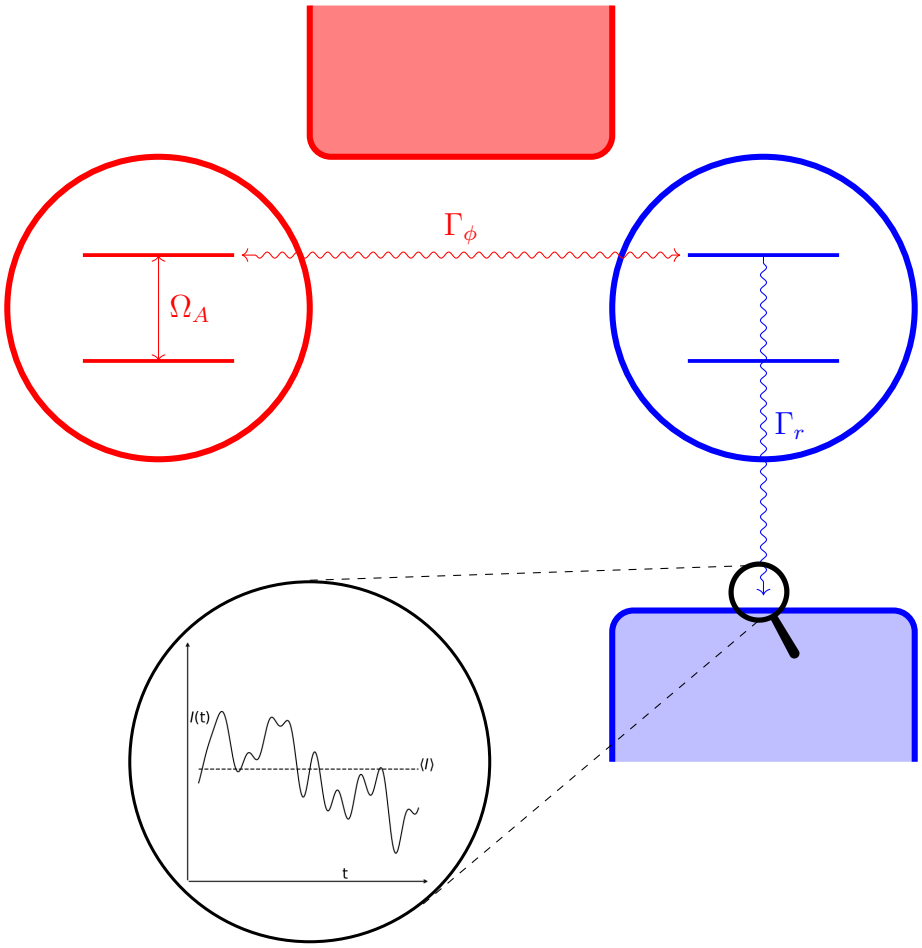

Measurements of heat current and its fluctuations in superconducting quantum systems

Master's thesis in Master Programme Physics

Ludvig Nordqvist

DEPARTMENT OF MICROTECHNOLOGY AND NANOSCIENCE
CHALMERS UNIVERSITY OF TECHNOLOGY
Gothenburg, Sweden 2025
www.chalmers.se

Master's thesis 2025

Measurements of heat current and its fluctuations in superconducting quantum systems

Ludvig Nordqvist

CHALMERS
UNIVERSITY OF TECHNOLOGY

Department of Microtechnology and Nanoscience
Quantum Technology Laboratory
202Q group
Chalmers University of Technology
Gothenburg, Sweden 2025

Measurements of heat current and its fluctuations in superconducting quantum systems
Ludvig Nordqvist

Supervisor: Simon Sundelin, Chalmers Tekniska Högskola
Examiner: Simone Gasparinetti, Chalmers Tekniska Högskola

Master's Thesis 2025
Department of Microtechnology and Nanoscience
Quantum Technology Laboratory
202Q-lab
Chalmers University of Technology
SE-412 96 Gothenburg
Telephone +46 31 772 1000

Cover: Schematic of the two qubit interaction which is set up and measured in this project.

Typeset in LaTeX
Printed by Chalmers Reproservice
Gothenburg, Sweden 2025

Measurements of heat current and its fluctuations in superconducting quantum systems

Ludvig Nordqvist
Department of Microtechnology and Nanoscience
Chalmers University of Technology

Abstract

As the quantum systems we can control and manipulate increase in size, understanding heat dynamics becomes increasingly important. In this master's project, we study the heat currents flowing between two out-of-equilibrium reservoirs across a superconducting quantum circuit composed of two mutually coupled, flux-tunable qubits. Electrical noise applied to the flux line of a qubit induces incoherent coupling between the modes in the single excitation manifold. Each mode is coupled to a thermal bath, realized with microwave waveguides. By coherently driving one of the modes to its first excited state, a heat current is induced. We measure heat currents on the scale of a few attoWatts, along with the fluctuations in said current. The results are compared to simulations that use full counting statistics to compute the currents and fluctuations of the process. These findings pave the way for demonstrating advantages of quantum systems over classical ones in quantum thermodynamics.

Keywords: Quantum, Quantum Thermodynamics, Power measurements, Circuit quantum electrodynamics, Current fluctuations, Thermodynamic Uncertainty relations, Heterodyne power fluctuations.

Acknowledgements

First of all I would like to thank my supervisor Simon Sundelin and examiner Simone Gasparinetti for their supervision. Without your support and many discussions this project would not have been possible. I would also like to thank Dr. Aamir Ali for his input and support through the course of this project. I also want to thank Dr. Mark Mitchinson and Khalak Mahadeviya of Trinity College Dublin for their theoretical support. Mark for providing the theoretical background for measuring the fluctuations in currents from a quantum system and Khalak for the software used to simulate the heat currents and fluctuations of the system using full counting statistics.
And to everyone in the 202Q-lab. Thank you for making these past months among the most enjoyable and rewarding of my academic journey. The fun and collaborative spirit that is ever present in the office makes it a joy to come in to the office every day.
And lastly, to the lifelong friends that I have made while studying at Chalmers. Thank you for always being there and making each day enjoyable.

Ludvig Nordqvist, Göteborg, August 2024

“Sikta mot stjärnorna”

så landar du kanske i trädtopparna...

Contents

List of Figures

List of Tables

1
Introduction

In the early twentieth century, physicists faced a problem where the theories of the time were in contradiction with observed phenomena. Among these were the ultraviolet catastrophe and the photo electric, effect neither of which could be described by classical theories. The effort of fixing the problems predicted by classical theories culminated in the idea of quantization, where energies come in discrete packets, called quanta, instead of existing in a continuum. The theory of quantum mechanics has since revolutionised physics and engineering. It has paved the way for developing new technologies such as the laser and transistor by providing a powerful framework explaining phenomena such as quantum tunneling and superposition.
One potential application of quantum mechanics was theorised by Richard Feynman In 1982. Feynman theorised that to more effectively simulate physics, which inherently is quantum mechanical, quantum mechanics could be utilised [1]. This sparked the idea of quantum computing, in which quantum mechanical coherence and entanglement is exploited to gain a computational advantage over classical computers. Mathematically this is represented as follows. The state of a general two level system is described by a state ket $|\psi\rangle$ in a Hilbert space H.

$$|\psi\rangle = \begin{pmatrix} \alpha \\ \beta \end{pmatrix}. \tag{1.1}$$

For a two level system this is typically referred to as a qubit, and in general a qudit for a d-level system. A composite system containing multiple qudits is described by the tensor product of the individual state kets. Taking the tensor product between two kets the increases the dimensionality of the new state vector through multiplication of the individual dimensions. For example, a system containing 2 qubits with states $|\psi_1\rangle$ and $|\psi_2\rangle$ is represented by

$$|\psi\rangle_{total} = |\psi_1\rangle \otimes |\psi_2\rangle = \begin{pmatrix} \alpha \\ \beta \end{pmatrix} \otimes \begin{pmatrix} \gamma \\ \delta \end{pmatrix} = \begin{pmatrix} \alpha\gamma \\ \alpha\delta \\ \beta\gamma \\ \beta\delta \end{pmatrix}, \tag{1.2}$$

which is a 4-dimensional object. Herein lies the potential of quantum computing. With a linear increase of the number of computational elements the computational space grows exponentially. But controlling single qubits is complicated. their interaction with the environment is a necessity for control of quantum quantum systems, but it causes their coherence times, the rate at which information is lost to the environment, to decrease significantly.

Peter Shor proved it's possible for quantum systems to showcase computational advantages over classical systems [2] being exponentially faster than classical systems at integer factorisation. This sparked a major interest in quantum computing. Since then quantum computing has gained much interest, both as a theoretical curiosity and as a potential new paradigm of computing. The first milestone towards building quantum computers was laid by Serge Haroche when he successfully isolated single photons and measured their interaction with atoms [3]. Since then larger quantum systems have been realised that can compute real world problems [4].

As quantum computing is explored it has been demonstrated that quantum systems can be operated as thermal machines that generate useful work [5]. And even experience thermal advantages over classical systems through violations of thermodynamic uncertainty relations or kinematic uncertainty relations [6, 7]. For this reason, the field of quantum thermodynamics has gained much attention in recent years.

Quantum thermodynamics is the study of quantities such as energy, currents and entropy production in quantum systems. It explores how quantum systems obey or deviate from classical thermodynamic principles. The field bridges the gap between quantum and classical systems by investigating how quantum effects such as coherence, entanglement, and superposition change thermal processes. Furthermore, quantum thermodynamics has significant implications for the future development of quantum computing. As we are able to control larger systems it is becoming increasingly important to understand how energy is distributed and transported in nanoscale devices. By understanding the thermodynamics of quantum systems we can better understand how quantum mechanical resources like superposition, coherence and entanglement can be utilized i quantum thermal machines.

In conclusion, the connection between quantum computing and quantum thermodynamics is not just a theoretical curiosity. To advance both fields the insights gained from further exploring quantum thermodynamics using superconducting qubits will play an essential role as we continue to engineer larger quantum systems to realise the full potential of quantum technologies.

1.1 Superconductivity

In 1911 Heike Kamerlingh Onnes discovered that when solid mercury is cooled to 4.2K it loses all electrical resistance. This is since known as superconductivity and is a phase transition that many metals can undergo. Materials that can transition into a superconducting state have been since been thoroughly studied and showcase many interesting phenomena. One such property of a superconductor is the Meissner effect which causes a superconductor to trap any magnetic flux which in present in when it surpasses the critical temperature [8]. Effectively expelling the magnetic field, as shown in figure 1.1.

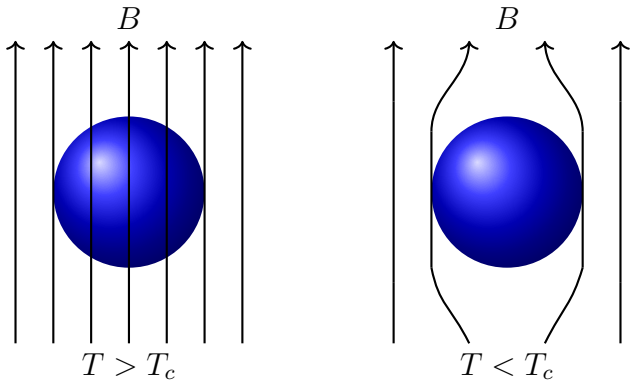

Figure 1.1: Magnetic field in a superconductor above and below the critical temperature.

According to BCS (Bardeen-Cooper-Schrieffer) theory, superconductivity is caused by the electrons forming Cooper pairs. Each Cooper pair consists of two electrons (fermions) that form a composite boson, condensing into a Bose-Einstein condensate at ultra-low temperatures. Although superconducting qubits are not the only way of realising isolated two level systems, it is one of the top contenders for near term large scale quantum computing due to the coherence times and energies associated with the SC-qubits being in the MHz range. Thus making the superconductor a key element in experiments with quantum systems.

1.1.1 The Josephson effect

The Josephson effect is a remarkable quantum phenomenon that occurs in superconducting materials, describing how currents move across thin insulating barriers in superconductors. It was originally theorised by Brian Josephson in 1962 [9]. The effect is derived by considering two superconductors isolated by a thin barrier as visualised in figure 1.2. This is called a Josephson junction. When a material undergoes a phase transition to its superconducting state, it can be described by a macroscopic wave function as a Bose-Einstein condensate.

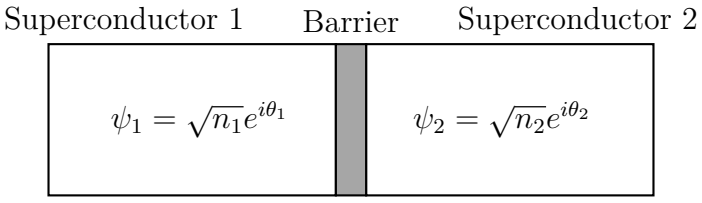

Figure 1.2: A schematic of a Josephson Junction, consisting of two superconductors separated by a thin insulating barrier.

We define the relative phase of the two superconductors as $\varphi = \theta_1 - \theta_2$. By solving the coupled Schrödinger equation of the two wave functions the expressions for the voltage and current across the junction are derived and given in given in equations 1.3 and 1.4 [8].

$$I = I_c \sin(\varphi(t)) \tag{1.3}$$

$$\frac{\partial \varphi}{\partial t} = \frac{2e}{\hbar} V(t) \tag{1.4}$$

I_c is the critical current at which the superconductor loses its superconducting property. It's a parameter dependent on the material and geometry of the junction. Combining the two equations we find that the inductance, $L = \frac{V}{\frac{dI}{dt}}$, across the junction is given by.

$$L(\varphi) = \frac{\phi_0}{I_c \cos(\varphi)}. \tag{1.5}$$

What is noteworthy about this is that the inductance is not linear. Allowing us to create non-linear circuit elements which, as we will see in section 2.2.4, is essential for engineering artificial atoms that are used to study quantum systems in this project.

2
Theory

In this chapter the needed theoretical knowledge for this thesis will be presented. The theory of quantum mechanics is introduced and used to quantize the circuit elements present on the device measurements are performed on. The interaction between light and matter is then explained and related to the area of quantum thermodynamics. Lastly the theoretical background for the measurements techniques applied in this thesis are presented.

2.1 Open quantum systems

The time evolution of a quantum mechanical state, often called a state ket, is governed by the Schrodinger equation [10]

$$i\hbar\frac{\partial}{\partial t}\left|\psi\right\rangle = \mathcal{H}\left|\psi\right\rangle. \tag{2.1}$$

While this equation correctly describes the evolution of a pure state $|\psi\rangle$ it is does not capture how mixed states evolve. A mixed state is described by it's density matrix $\rho = \sum_i p_i \left|\psi_i\right\rangle \left\langle\psi_i\right|$, where p_i is the probability of the system being in the state $|\psi_i\rangle$. To this end the "Von neumann" equation is used [11]. The time evolution of the density operator ρ of a system is given by

$$\frac{d\rho}{dt} = -\frac{i}{\hbar}[\mathcal{H}, \rho]. \tag{2.2}$$

where and $[A, B] = AB - BA$ represents the commutator between two operators. Despite being an improvement over the Schrodinger equation the Von neumann equation still has limitations. Namely it's limited by the being computationally difficult to solve for large quantum systems as the degrees of freedom increases quickly with the size of the system. An example of such a system is a quantum system in contact with an environment, which can be infinitely large. To this end the evolution of such systems is modeled by the "Gorini – Kossakowski – Sudarshan – Lindblad" (GKSL) equation instead [12]. The GKSL equation describes how a quantum system in contact with a Markovian environment evolves in time. Where a Markovian environment is equivalent to the environment being memory less. This is usually referred to as an open quantum system. In deriving the equation the Hamiltonian is split into 3 parts. One part describing the system, a bath representing a large environment to which information is lost and term that captures the interaction between the bath and system

$$\mathcal{H} = \mathcal{H}_\mathcal{S} + \mathcal{H}_\mathcal{B} + \mathcal{H}_\mathcal{I}. \tag{2.3}$$

Under the assumption that the system and bath are weakly coupled, and the Markovian approximation is valid, the evolution of the density operator is then given by

$$\frac{d\rho}{dt} = -\frac{i}{\hbar}[\mathcal{H}, \rho] + \sum_{\alpha} \mathcal{D}[L_\alpha]\rho, \tag{2.4}$$

where the super operators $\mathcal{D}[L_\alpha]\rho = L_\alpha \rho L_\alpha^\dagger - \frac{1}{2}\{L_\alpha^\dagger L_\alpha, \rho\}$ are the dissipators modeling loss of information to the environment. This dissipator is said to be on Lindblad form. If there are no dissipators, i.e. no information of the system is lost to the environment, the Lindblad equation is reduced to the Von Neumann equation. Each dissipator has an assosciated decay rate Γ_i representing the rate at which information is lost to the environment. This is the most general form of a Markovian master equation[13]. If we consider a two level system coupled to an environment the dynamics of it and it's interaction with the environment is fully captured by the operators $\sigma^+, \sigma^-, \sigma_x$ that span the vector space $\mathbb{C}^{2x2}$ corresponding to dephasing, excitation and relaxation of the system.

2.2 Circuit quantisation

Circuit quantum electrodynamics (circuit QED) is the study of 2-dimensional electrical circuits with where quantum mechanical effects significant impact the dynamics of the system. In circuit QED the properties of superconducting materials are exploited to realise quantum mechanical phenomena. The device used in this thesis is such a device, realised on a circuit QED platform. In this section the quantisation of the circuit components of the device of interest are computed and their equations of motion derived. The qubits on the sample are of the "transmon" type. The transmon, first theorised by Koch et al. in 2007 [14] and realised in the same year [15], is a candidate for realising scalable quantum computers as the coherence times of the transmon are long and gate times short, allowing both control and measurement of the device of interest. In this section quantisation of electrical circuits will be introduced and the dynamics of the relevant circuit elements derived. These include the LC-oscilator, the Transmon and the waveguides used for interacting with the circuit elements.

2.2.1 Linear circuit elements

To determine the equations of motion of a circuit it is desirable to find the generalised coordinates of the system. We first consider the energy and magnetic flux stored in a circuit element [16]

$$E(t) = \int_{-\infty}^{t} I(t')V(t')dt' \tag{2.5}$$

$$\phi(t) = \int_{-\infty}^{t} V(t')dt'. \tag{2.6}$$

Combining equation 2.5 and 2.6 with $V = L\frac{dI(t)}{dt}$ and $I = C\frac{dV(t)}{dt}$ we find the energy stored in a capacitance and inductance given in table 2.1 .

Circuit Element	Symbol	Energy
Capacitance		$\frac{1}{2}C\dot{\phi}^2$
Inductance		$\frac{1}{2L}\phi^2$

Table 2.1: Linear circuit elements and the energy stored in them.

In analogy to classical mechanics the energy stored in a capacitance is interpreted as a kinetic energy and the energy stored in a inductance as a potential energy. With this in hand we are ready to quantise circuit elements.

2.2.2 Quantisation of the LC oscillator

With the energies of the inductance and capacitance as described in table 2.1 we consider the LC circuit shown in figure 2.1. Consisting of a capacitor and inductance in series the Lagrangian takes following form:

$$\mathcal{L} = \frac{1}{2}C\dot{\phi}^2 - \frac{1}{2L}\phi^2. \tag{2.7}$$

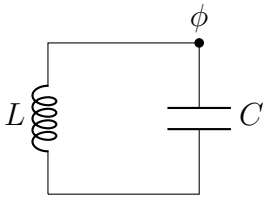

Figure 2.1: Circuit diagram of a LC circuit. ϕ represents the node flux in that point as defined in equation 2.6.

As the equations of motion in quantum mechanics typically are given in a Hamiltonian formalism we are interested in the Hamiltonian of this system. The Hamiltonian $\mathcal{H}$ is a function of the canonical momentum and the node flux. To this end a Legendre transformation is performed to find the canonical momentum p_n of the system [17]. The Hamiltonian is related to the Lagrangian through the Legendre transformation:

$$\mathcal{H} = \sum_{i=1}^{n} p_n\dot{\phi}_n - \mathcal{L}. \tag{2.8}$$

Where p_n is the canonical momentum defined as

$$p_n = \frac{\partial\mathcal{L}}{\partial\dot{\phi}_n}. \tag{2.9}$$

In the case of the LC circuit, where there is only one node flux, we find that

$$p_n = p = \frac{\partial\mathcal{L}}{\partial\dot{\phi}} = C\dot{\phi}. \tag{2.10}$$

and

$$\mathcal{H} = C\dot{\phi}\dot{\phi} - \mathcal{L} = \frac{p^2}{2C} + \frac{\phi^2}{2L}. \tag{2.11}$$

The form of this Hamiltonian is much like that of the harmonic oscillator $\mathcal{H} = \frac{p^2}{2m} + \frac{m\omega^2 x^2}{2}$. By interpreting the capacitance as the mass we find the frequency of the circuit as $\omega = \frac{1}{\sqrt{LC}}$. The variables p and ϕ are promoted to quantum mechanical operators as

$$\begin{aligned} p &\to \hat{p} \\ \phi &\to \hat{\phi} \end{aligned} \tag{2.12}$$

and the canonical commutation relation is imposed on them such that:

$$[\hat{\phi}, \hat{p}] = i\hbar. \tag{2.13}$$

We define a set of operators usually referred to as "ladder operators" or annihilation operators $a, a^\dagger$. They are defined in terms of $\hat{p}$ and $\hat{\phi}$ where:

$$\hat{\phi} = \sqrt{\frac{\hbar}{2C\omega}}(a^\dagger + a) \tag{2.14}$$

$$\hat{p} = i\sqrt{\frac{\hbar C\omega}{2}}(a^\dagger - a). \tag{2.15}$$

The ladder operators fulfil the the following eigenvalue equations:

$$a\,|n\rangle = \sqrt{n}\,|n-1\rangle \tag{2.16}$$

$$a^\dagger\,|n\rangle = \sqrt{n+1}\,|n+1\rangle \tag{2.17}$$

where n represents the number of quanta in the circuit. By combining equations 2.16 and 2.17 a third eigenvalue equation is found

$$a^\dagger a\,|n\rangle = N\,|n\rangle = n\,|n\rangle\,. \tag{2.18}$$

This is an important since N is an hermitian operator such that $N = N^\dagger$. Meaning that the eigenvalues represents observable quantities that can be measured. It is convenient to rewrite the Hamiltonian in terms of this operator. Using that the commutator between the ladder operator fulfills the bosonic commutation relation $[a, a^\dagger] = 1$ the Hamiltonian for quantum mechanical LC oscillator takes the following form:

$$\mathcal{H} = \hbar\omega(N + \frac{1}{2}). \tag{2.19}$$

2.2.3 Quantisation of an infinite transmission line

The circuit elements are controlled using room temperature electronics that generate microwaves. The microwaves travel through a transmission line to the circuit in the dilution refrigerator, where they interact with the device of interest. The transmission line, or wave guide can be considered to be a infinite line of capacitors and inductances coupled in parallel as shown in figure 2.2.

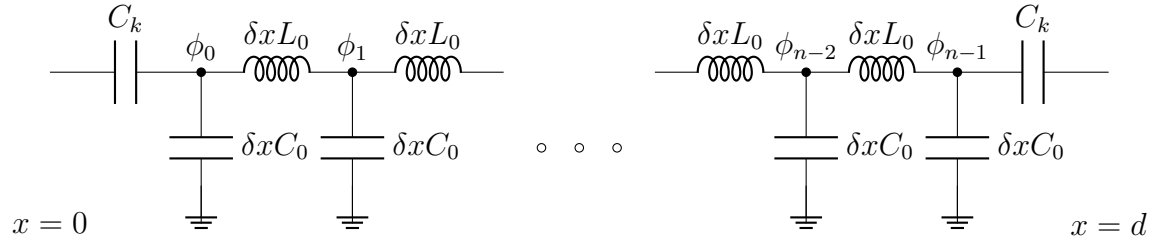

Figure 2.2: Circuit representation of a transmission line of length d. Each capacitance is separated by a distance δx.

The Lagrangian of the system is equivalent to a series of coupled LC-oscillators where the Lagrangian is the sum taken over all energy contributions [17].

$$\mathcal{L} = \sum_n \left(\frac{1}{2} \Delta x C_o \dot{\phi}_n^2 - \frac{1}{2} \frac{(\phi_n - \phi_{n-1})^2}{\Delta x L_0} \right) \tag{2.20}$$

By going in to the continuum limit where $\delta x \to 0$ the sum is replaced by an integral such that

$$\mathcal{L} = \int_{-\infty}^{\infty} dx \frac{C_0}{2} \left(\frac{\partial \phi(x,t)}{\partial t} \right)^2 + \frac{1}{2L_0} \left(\frac{\partial \phi(x,t)}{\partial x} \right)^2 . \tag{2.21}$$

The equations of motion are regained by applying the Euler-Lagrange equation. We find that

$$\frac{\partial^2 \phi(x,t)}{\partial t^2} - c^2 \frac{\partial^2 \phi(x,t)}{\partial x^2} = 0 \tag{2.22}$$

which is just the wave equation of light, where c corresponds to the speed of light in the medium. Once again performing a Legendre transformation of the Lagrangian, [2.8, 2.9] we regain the Hamiltonian in the continuum limit as

$$\mathcal{H} = \int_{-\infty}^{\infty} dx \frac{1}{2C_0} p^2(x,t) + \frac{1}{2L_0} \left(\frac{\partial \phi(x,t)}{\partial x} \right)^2 . \tag{2.23}$$

Where the canonical commutation is imposed on p, ϕ such that

$$[\phi(x,t), \phi(x',t')] = [p(x,t), p(x',t')] = 0 \tag{2.24}$$

and

$$[\phi(x,t), p(x',t')] = i\hbar \delta(x - x') \delta(t - t'). \tag{2.25}$$

By expressing the flux field ϕ and charge density p in terms of their Fourier transform

$$\phi(x,t) = \frac{1}{\sqrt{2}} \int_{-\infty}^{\infty} \phi(k,t) \exp(ikx) \tag{2.26}$$

$$p(x,t) = \frac{1}{\sqrt{2}} \int_{-\infty}^{\infty} p(k,t) \exp(ikx) \tag{2.27}$$

the solution of $\phi(k,t)$ is

$$\frac{\partial \phi(k,t)}{\partial t^2} + \omega_k \phi(k,t) = 0, \tag{2.28}$$

where $\omega_k = ck = \frac{k}{\sqrt{C_0 L_0}}$ and k is the wave number. By introducing annihilation and creation operators that obey the bosonic commutation relations,

$$[a_i, a_j^\dagger] = \delta_{ij} \tag{2.29}$$

$$[a_i, a_j] = 0. \tag{2.30}$$

The flux and charge operators can be expressed as

$$\phi(k,t) = \sqrt{\frac{\hbar}{2C_0\omega_k}}(a_{-k}^\dagger(t) + a_k(t)) \tag{2.31}$$

$$p(k,t) = i\sqrt{\frac{\hbar C_0\omega_k}{2}}(a_{-k}^\dagger(t) - a_k(t)). \tag{2.32}$$

Inserting these in to 2.26 and 2.27 we find that

$$\mathcal{H} = \hbar\int_{-\infty}^{\infty} dk \left(a_k^\dagger a_k + \frac{1}{2}[a_k, a_k^\dagger]\right)\omega_k = \hbar\int_{-\infty}^{\infty} dk \left(a_k^\dagger a_k + \frac{1}{2}\delta(0)\right)\omega_k. \tag{2.33}$$

The Hamiltonian is the sum of an infinite set of electromagnetic modes plus the zero point energy of each mode. Mathematically this is equivalent to a bath of harmonic oscillators supporting all mode frequencies equally. The zero point energy has no meaningful contribution to the dynamics of the system and can thus be disregarded going forward.

2.2.4 The transmon

For realising near term quantum computing the transmon is one of the most promising candidates. Originally theorised by Koch et al. [14] it has since been thoroughly studied and major advances in quantum computing have been achieved using it. The transmon, whose energy spectrum resembles that of an atom, is an LC oscillator where the linear inductance is replaced by a Josephson junction. Due to the non linearity of the energy spectrum, the transmon is can also be referred to as an artificial atom. The behaviour of the Josephson junction is captured by the two Josephson relations found by Brian Josephson described in detail in chapter 1.1.1. The non linearity in the energy spectrum is important because it makes the higher level transitions have a different transition frequency than the first excited state. Essentially, creating a two level system that can be manipulated. Below is the circuit representation of a transmon qubit.

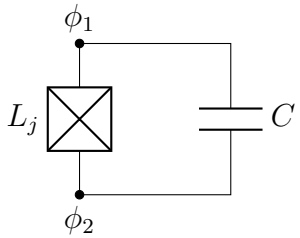

Figure 2.3: Circuit representation of a transmon. The component on the left is a Josephson junction shunted by a capacitance.

The Josephson inductance can be defined as

$$L_j = \frac{\phi_0}{2\pi I_c} \frac{1}{\cos(2\pi\phi/\phi_0)}. \tag{2.34}$$

If the linear inductance of the LC-oscillator is replaced by the Josephson inductance this causes the energy levels to shift as a function of the flux variable ϕ. The energy stored in the Josephson inductance is [18]

$$E = I_c \int dt(\frac{d\phi}{dt}) \sin(\frac{2\pi\phi}{\phi_0}) = -\frac{\phi_0 I_c}{2\pi} \cos(\frac{2\pi\phi}{\phi_0}) = -E_j \cos(\frac{2\pi\phi}{\phi_0}). \tag{2.35}$$

By replacing the linear inductance energy term in the Hamiltonian of the LC-oscillator with this and adding the shunting capacitance C_s to the total capacitance, $C_\Sigma = C + C_s$, the Hamiltonian of the circuit reads

$$\mathcal{H} = \frac{(Q - Q_g)^2}{2C_\Sigma} - E_j \cos(\varphi) = 4E_c(n - n_g) - E_j \cos(\varphi), \tag{2.36}$$

where $\varphi = \frac{2\pi\phi}{\phi_0}$, E_c is the capacative energy defined as $E_c = \frac{e^2}{2C_\Sigma}$, n is the number operator and n_g is an offset in the energy caused by the shunting capacitance. For a qubit to the operationally viable we wish for it to have large anharmonicity $\alpha = \omega_{01} - \omega_{12}$ as a means to be able to drive the first transition without risk of also exciting to the second excited state.

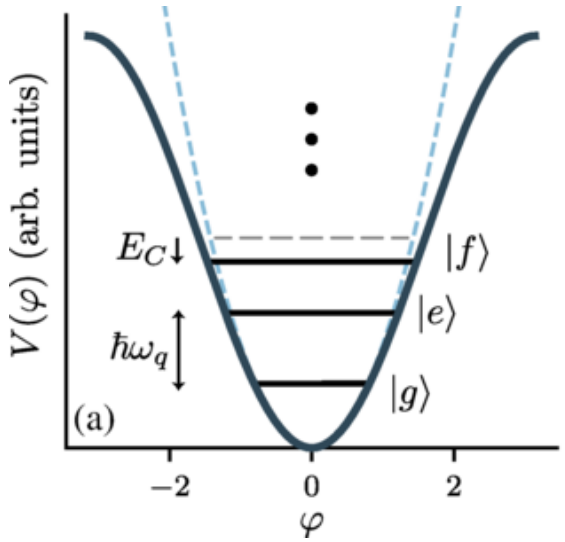

Figure 2.4: Energy spectrum of a transmon (Blue line) and a LC oscillator (dashed lines) showing how a JJ alternates the energy spectrum of an LC-oscillator. Image taken from [18].

There is also a need for it to be insensitive to varying values of n_g as this value, dependent on the tunneling of cooper pairs through the JJ, cannot easily be controlled. The qubits susceptibility to the charge offset is captured by the ratio of E_j and E_C.

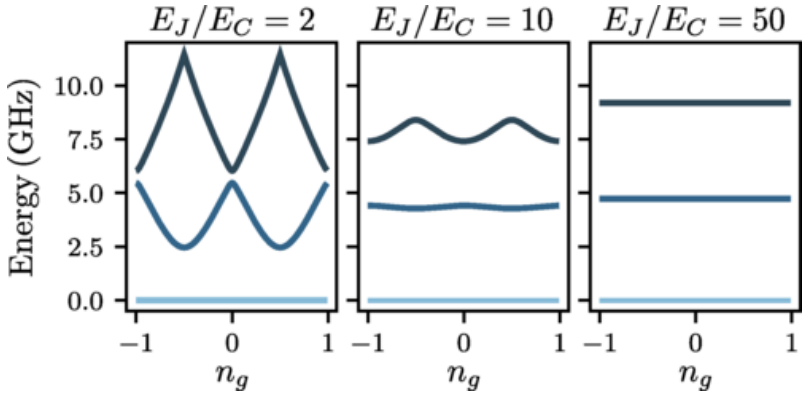

Figure 2.5: Frequency dependence of the first three energy levels of the transmon as a function of n_g. For larger values of E_J/E_C the energy levels are less sensitive to changes in n_g while the anharmonicity also decreases with this ratio. Image taken form [18].

As shown in figure 2.5 the ratio $\frac{E_j}{E_C}$ is crucial for having a stable qubit whose frequency doesn't shift due to cooper pairs tunneling through the junction.
The reason being that the charge-sensitivity is exponentially suppressed while the anharmonicity is only linearly suppressed. Allowing for qubits with low charge sensitivity while retaining a anharmonicity in the range of $\sim 100s$ of MHz. So for practical purposes it's useful to work in a regime where this ratio is large [14] . To better understand the behaviour of the transmon it is useful to express the Hamiltonian in terms of the ladder operators. This is done by taylor expanding the cosine term in 2.36 to fourth order and expressing the operators ϕ, n in terms in ladder operators and approximating the terms with unequal number of createion/anihilation operators to be 0. This leads to the Hamiltonian taking the following form:

$$\mathcal{H} = \hbar\omega_a a^\dagger a - \frac{E_c}{2} a^\dagger a^\dagger a a, \tag{2.37}$$

where $\omega_a = \sqrt{8E_C E_j} - E_c$.

2.3 Light matter interaction

With the transmon and wave guide introduced we are now ready to discuss how they interact and the many interesting phenomena that can be studied in such systems. We will first introduced the Jaynes-Cummings model that captures how a transmon and transmission line interact. We will then derive the emission spectrum of a a two level system and explain it in terms of both the eigenmodes of the Hamiltonian and spectral density. Lastly the theory of two artificial atoms interacting is covered.

2.3.1 The Jaynes-Cummings model

The Jaynes-Cummings model was developed in the 1960s by Edwin Jaynes and Fred Cummings. It's an effective theory for describing an atom interacting with a single mode of a electromagnetic field. The case generally considered is an atom

coupled to a cavity with a single quantised mode of a electromagnetic field [2]. The Hamiltonian of this system is [19]

$$\mathcal{H} = \frac{\hbar\omega_a}{2}\sigma_z + \hbar\omega_c a^\dagger a + \hbar g(\sigma_+ + \sigma_-)(a^\dagger + a). \tag{2.38}$$

The Hamiltonian has three parts to it. The first term is the familiar two level-system atom with frequency ω_a. The second term is a single mode of the electromagnetic field of the cavity, and the last term is the interaction between the atom and cavity. By moving in to a rotating frame and applying the rotating wave approximation (RWA) , where quickly rotating terms oscillating with frequency $\pm(\omega_a + \omega_c)$ are disregarded, the Hamiltonian takes the following form:

$$\mathcal{H} \to \tilde{\mathcal{H}}_{\mathcal{JC}} = \frac{\hbar\omega_a}{2}\sigma_z + \hbar\omega_c a^\dagger a + \hbar g(\sigma_+ a + \sigma_- a^\dagger). \tag{2.39}$$

This is the famous Jaynes-Cummings Hamiltonian. The interaction term describes the events that can take place between the coupled systems. It allows for exchange of photons between the cavity and the atom through the states $|g\rangle\,|n+1\rangle \leftrightarrow |e\rangle\,|n\rangle$, captured by $\sigma_- a^\dagger$ and its hermitian conjugate $\sigma_+ a$. The other terms in the interaction Hamiltonian that where approximated be zero in the RWA describe two photon processes where the number of photons is not conserved. The RWA approximation is justified as the quickly rotating terms average to 0 in a weak coupling regime ($g \ll \omega_a$) where the atom and cavity are near resonance ($\omega_c \approx \omega_a$). The Jaynes-Cummings Hamiltonian conserves the number of quanta and it's Hilbert space is spanned by the states with eigenvalues

$$E_{n\pm} = \hbar\omega_c(n + \frac{1}{2}) \pm \frac{\hbar}{2}\sqrt{\Delta^2 + 4g^2(n+1)} \tag{2.40}$$

corresponding to the states

$$|n, +\rangle = \cos(\theta_n)\,|e, n\rangle + \sin(\theta_n)\,|g, n+1\rangle\,, \tag{2.41}$$

$$|n, -\rangle = -\sin(\theta_n)\,|e, n\rangle + \cos(\theta_n)\,|g, n+1\rangle \tag{2.42}$$

where Δ is the detuning between the atom and field and θ_n is the mixing angle defined as $\theta_n = \arctan(\frac{2g\sqrt{n+1}}{\Delta})$ [20].

2.3.2 Power spectral density of an atom

The emission spectrum of an atom subject to a source of light differs from that of an atom in vacuum, as can be understood in terms of the eigenvalues of the Jaynes Cummings Hamiltonian. See equation 2.40. By considering the Hamiltonian of a two level atom coupled to a coherent light source the emission spectrum, or resonance fluorescence can be calculated as the Fourier transform of the two point correlator $\langle\sigma^+(\tau)\sigma(0)\rangle$. The Hamiltonian is in a frame rotating at the cavity frequency ω_c is given by

$$\mathcal{H} = \frac{\Delta}{2}\sigma_z + \frac{\Omega}{2}(\sigma_+ + \sigma_-). \tag{2.43}$$

Δ is the detuning between the driving field and the atom frequency $\Delta = \omega_p - \omega_a$. By assuming a thermal population of 0 ($N = 0$) and solving the master equation

$$\frac{d}{dt}\rho = -i[\mathcal{H}, \rho] + \Gamma_1 \mathcal{D}[\sigma_-]\rho + \frac{\Gamma_\phi}{2}\mathcal{D}[\sigma_z]\rho \tag{2.44}$$

the two point correlator can $\langle \sigma^+(\tau)\sigma(0)\rangle$ be determined. The steps includes going in the long time limit and applying the quantum regression theorem to the expectation values of σ_-, σ_+ extracted from ρ. The interested reader is referred to [17] and the supplementary material in[21] for a an in depth derivation. By assuming a high pump power ($\Omega \gg \Gamma_1, \Gamma_2$) the resonant fluorescent spectrum is in a reflection measurement analytically expressed as

$$S_i(\omega) \approx \frac{1}{2\pi}\frac{\hbar\omega_a\Gamma_r}{4}\left\{\frac{\Gamma_s}{(\delta\omega_a + \Omega)^2 + \Gamma_s^2} + \frac{2\Gamma_2}{(\delta\omega_a)^2 + \Gamma_2^2} + \frac{\Gamma_s}{(\delta\omega_a - \Omega)^2 + \Gamma_s^2}\right\}. \tag{2.45}$$

The expression in equation 2.45 is remarkably simple as it's just a sum of 3 Lorentzians centered around the atom frequency ω_a, with a common pre-factor. This is commonly referred to as the "Mollow triplet". The units of the resonant fluorescent spectrum, or power spectral density (PSD) is [Energy/Hz/S]. A s the name suggests, it describes the density of the power of the atoms photon emission in the frequency domain. The center and side bands are separated by Ω as can be seen in equation 2.45

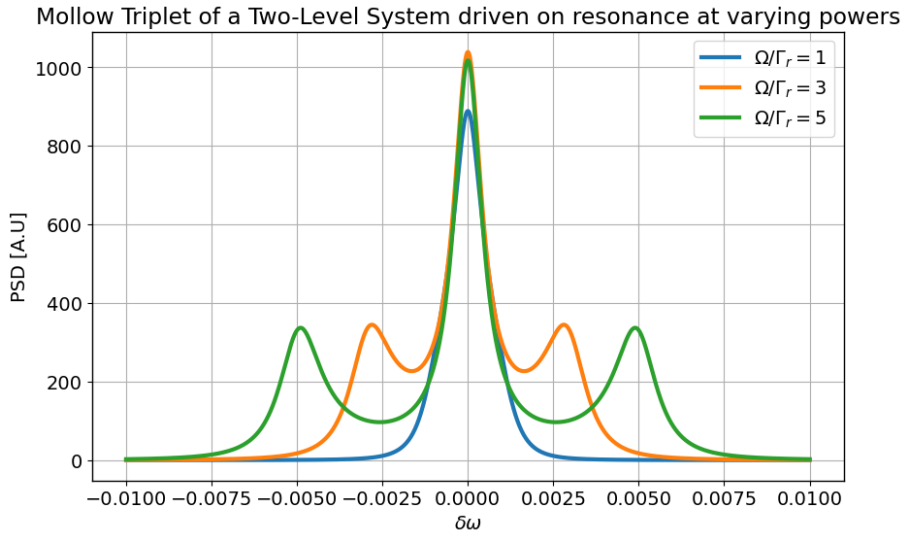

Figure 2.6: Plot of the mollow triplet driven at varying powers Ω.

The expression for the fluorescent emission of a two level system can also be understood by considering the energy levels of the atom coupled to coherent light source. The energy levels of this system are described by the number of photons and the state of the atom. In a given energy manifold the vector space is spanned by the states

$$\varepsilon(n) = \{|g, n+1\rangle, |e, n\rangle\}. \tag{2.46}$$

As was shown in section 2.3.1 these eigenstates are shifted when subject to a strong coherent field. The new eigenstates in the dressed basis when $\Delta = 0$ are given by

$$|\pm, n\rangle = \frac{|g, n+1\rangle + |e, n\rangle}{\sqrt{2}}. \tag{2.47}$$

The energy diagram of this Hamiltonian is shown in figure 2.7 where the possible transitions are indicated with arrows. This is in agreement with the expression for the fluorescent emission derived in equation 2.45 which indicates emission centered at 3 frequencies.

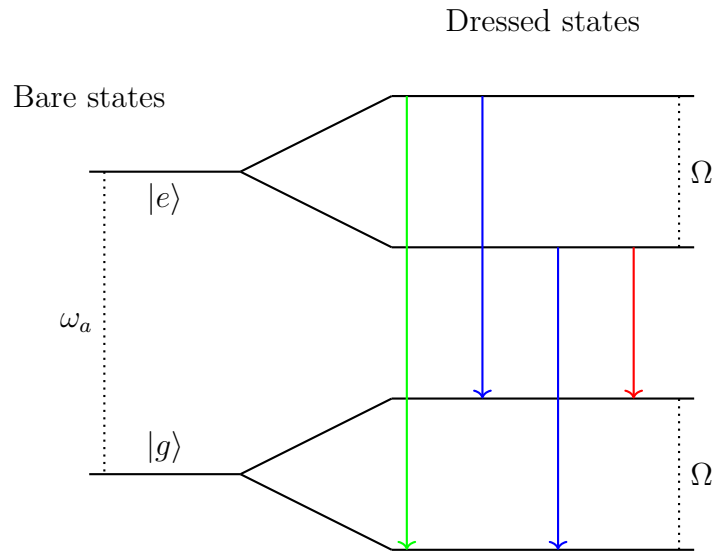

Figure 2.7: Figure showingcasing the possible transitions in a given energy manifold of a TLS subject to a coherent field. Transitions with the same color have of the same frequency.

By considering the dressed states it becomes clear that in the frequency domain 3 peaks will be visible. Each centered at $\omega = \omega_a \pm \Omega$ and one between, centered at $\omega = \omega_a$.

2.3.3 Atom-atom interactions

The system investigated in this thesis consists of two interacting flux tunable artificial atoms. The flux tunability of the qubits is realised by exchanging the single Josephson junction of the transmon with a Superconducting Quantum Interference Device (SQUID) [16]. The SQUID operates much like a JJ with the difference that the inductance is dependent on an external magnetic flux ϕ. The Hamiltonian of this scenario resembles that of the Jaynes-Cummings Hamiltonian with the modification that the bosonic creation/annihilation operators describing the light are exchanged with its qubit equivalence. The resulting Hamiltonian is given by

$$\mathcal{H} = \sum_{i=1}^{2} \frac{\hbar\omega_i(\phi)}{2}\sigma_i^\dagger\sigma_i + \hbar g(\sigma_1^\dagger\sigma_2 + \sigma_2^\dagger\sigma_1). \tag{2.48}$$

To find the eigenvalues the Hamiltonian is diagonalized by introducing the operators $\sigma_S = (\sigma_1 + \sigma_2)\sqrt{2}$ and $\sigma_A = (\sigma_1 - \sigma_2)/\sqrt{2}$. The subsript A/S indicates whether the operator is symmetric/anti-symmetric under the parity operator. Expressed in this basis the Hamiltonian is

$$\mathcal{H} = \hbar\tilde{\omega_1}(\phi)\sigma_S^\dagger\sigma_S + \hbar\tilde{\omega_2}(\phi)\sigma_A^\dagger\sigma_A. \tag{2.49}$$

Where the new frequencies of the modes are given by

$$\tilde{\omega_1}(\phi) = \frac{1}{2}(\omega_1(\phi) + \omega_2(\phi) + \sqrt{\Delta^2 + 4g^2}) = \omega_S \tag{2.50}$$

$$\tilde{\omega_2}(\phi) = \frac{1}{2}(\omega_1(\phi) + \omega_2(\phi) - \sqrt{\Delta^2 + 4g^2}) = \omega_A. \tag{2.51}$$

These will henceforth be referred to as the symmetric and anti-symmetric modes. This is an important result as the only measurable in quantum mechanics are eigenstates of hermitian operators. So when probing the system these are the qubit frequencies that will be measurable. From this it's possible to determine the coupling strength g between 2 qubits by through a measurement of the dressed state frequencies, as ω_S and ω_A differ by two times the coupling strength $2g$ on resonance.

$$\omega_S(\phi) - \omega_A(\phi) = [\Delta = 0] = 2g. \tag{2.52}$$

2.4 Input-output theory

Input-output theory is a framework for connecting the output of a quantum system to the input. It's a powerful tool which helps in understanding how to probe a quantum system. Within the scope of this thesis, it is used to characterize the device and find its eigenmodes and decay rates. The derivation of the input-output relations for a reflection measurement closely follows those given in [17, 22, 23]. In input output theory we consider a system given by the Hamiltonian

$$\mathcal{H} = \mathcal{H}_\mathcal{S} + \mathcal{H}_\mathcal{B} + \mathcal{H}_\mathcal{I}. \tag{2.53}$$

Capturing the dynamics of the system, the bath which the system is connected to and the interaction between the system and bath. When modeling a two-level system coupled to a transmission line as in 2.33. The Hamiltonians are given by

$$\mathcal{H}_S = \frac{\hbar\omega_a}{2}\sigma_z, \tag{2.54}$$

$$\mathcal{H}_B = \int_0^\infty d\omega\omega b^\dagger(\omega)b(\omega), \tag{2.55}$$

$$\mathcal{H}_I = \int_0^\infty d\omega\sqrt{\frac{\Gamma(\omega)}{2\pi}}\left(b^\dagger(\omega)\sigma_- + \sigma_+ b(\omega)\right). \tag{2.56}$$

$b^\dagger(\omega), b(\omega)$ are the bosonic creation/annihilation operators that create an excitation at ω and $\mathcal{H}_I$ captures that the system can either absorb a photon from the environment or emit a photon to the bath. The rate at which this occurs given by $\Gamma(\omega)$.

To find the relation between the input field and the output a few assumptions are made. $\Gamma(\omega)$ is assumed to be independent of ω and the lower integration limits are extended to $-\infty$. These assumptions are justified because $\omega_a \gg \Gamma$ and only terms with frequencies close to ω_a are relevant. The Heisenberg equations of the operators are calculated and read

$$\dot{b} = -i\omega b(\omega) - i\sqrt{\frac{\Gamma}{2\pi}}\sigma_-, \tag{2.57}$$

$$\dot{\sigma}_- - i\omega_a\sigma_- + i\sigma_z\sqrt{\frac{\Gamma}{2\pi}}\int_{-\infty}^{\infty} d\omega b(\omega). \tag{2.58}$$

The operators $b_{in}(\omega,t), b_{out}(\omega,t)$ are defined that describe the bath at a previous or future time. They depend on t_0 or t_1, where $t_0 < t$ and $t_1 > t$ and are given by

$$b_{in}(\omega,t) = \frac{1}{\sqrt{2\pi}}\int_{-\infty}^{\infty} d\omega b(\omega,t_0)\exp\left(-i\omega(t-t_0)\right) \tag{2.59}$$

$$b_{out}(\omega,t) = \frac{1}{\sqrt{2\pi}}\int_{-\infty}^{\infty} d\omega b(\omega,t_1)\exp\left(-i\omega(t-t_1)\right). \tag{2.60}$$

combined with the Heisenberg equations of motion and a bit of algebra we are able to relate $b_{out}(\omega,t)$ to $b_{in}(\omega,t)$ as

$$b_{out}(\omega,t) = b_{in}(\omega,t) - i\sqrt{\Gamma}\sigma_-. \tag{2.61}$$

This is an important result as it can be used to probe the system. When considering a coherent probing tone on the steady state of the system the field operators are modified to $\alpha_{in/out} = \langle b_{in/out}\rangle$ and equation 2.61 is modified to

$$\alpha_{out}(\omega,t) = \alpha_{in}(\omega,t) - i\sqrt{\Gamma}\langle\sigma_-\rangle, \tag{2.62}$$

where $\langle\sigma_-\rangle$ can be calculated from the steady state solution of ρ as $\langle\sigma_-\rangle = \mathrm{Tr}\{\sigma_-\rho\} = \rho_{01}$.

2.4.1 Spectroscopy

For probing the system we need to interact with the system and have some way of determining how that interaction changes the output. In this project the system is characterized by sending coherent tones to the system and measuring the reflection. This is realised using a Vector Network Analyzer (VNA) which measures the reflection

$$r = \frac{\alpha_{out}}{\alpha_{in}} \tag{2.63}$$

of a coherent tone. The case of a waveguide coupled to a qubit is shown in figure 2.8.

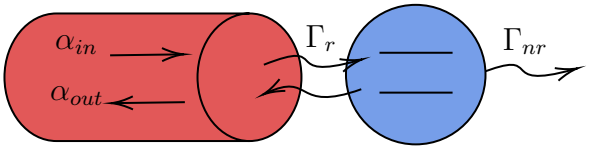

Figure 2.8: A waveguide populated with a field coupled to a two level system with radiative decay rate Γ_r and non-readiative decay rate Γ_{nr}. The field operators $\alpha_{in/out}$ represent the incoming/outgoing field of a coherent tone that are measured using a VNA.

The system we are probing is a qubit coupled to the end of a wave guide. The equations connecting the input and output of such a system were derived in section 2.4. Combining equations 2.62 and 2.63 we find that

$$r = 1 - i\Gamma\frac{\langle\sigma_-\rangle}{\alpha_{in}}. \tag{2.64}$$

Combining the expression for $\langle\sigma_-\rangle$ derived in the supplementary material of Lu et. al. [21] with a coherent probing field described by $\alpha_{in} = \frac{\Omega}{2\sqrt{\Gamma_r}}$, the reflection becomes

$$r = 1 - \frac{i\Gamma_r\Gamma_1(\delta\omega - i\Gamma_2)}{\Omega^2\Gamma_2 + \Gamma_1(\delta\omega^2 + \Gamma_2^2)}. \tag{2.65}$$

where $\delta\omega = |\omega_p - \omega_a|$ is the detuning between the probing field and the atom, and Γ_1, Γ_2 are the decoherence rates of the atom defined as $\Gamma_1 = \Gamma_r + \Gamma_{nr}$ and $\Gamma_2 = \frac{\Gamma_1}{2} + \Gamma_\phi$. The reflection is shown for varying probing power in figure 2.9. It's worth noticing that there is a power at which the reflection is almost equal to zero on resonance. This is called the magic power. The reason for this is that at this power the atom is coherently driven to it's excited state. The qubit then emits photons back to the wave guide with an exact opposite phase of the incoming field that destructively interact with the incoming field, resulting in the reflection begin nearly equal to zero.

The phase of the reflection is shown in figure 2.10. As can be seen the phase does a complete phase shift when the qubit is probed at the "magic power" or lower. As the power increases the phase is closer to 0 as the incoming field "overpowers" the emission of photons from the qubit. This can be understood by looking at the second term in equation 2.65. As Ω increases the ratio becomes smaller and the total reflection approaches unity.

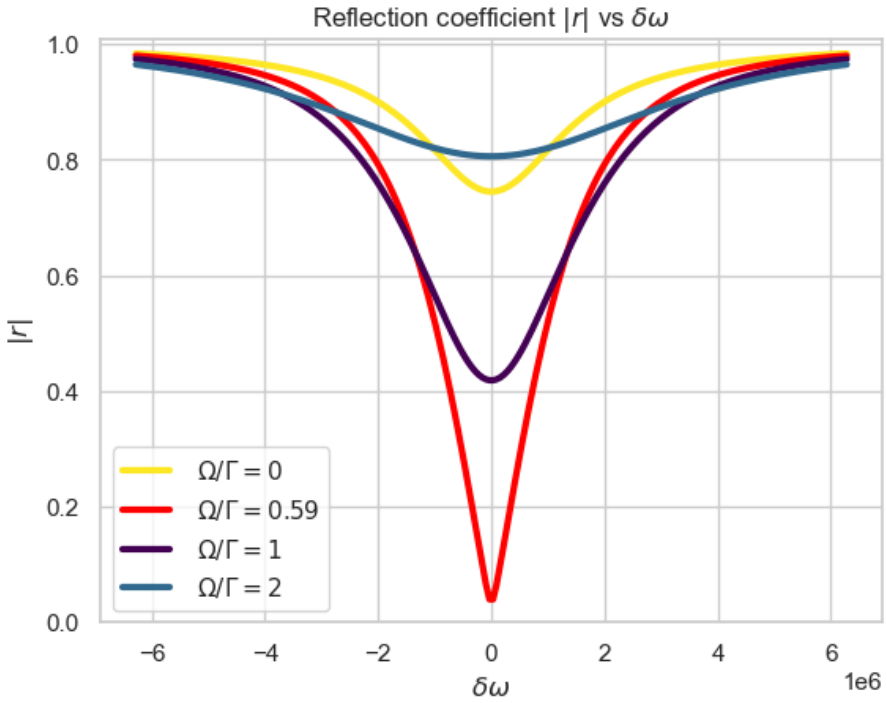

Figure 2.9: The magnitude of the reflection $|r|$ as a function of the detuning between the atom and probe frequency at varying probing powers.

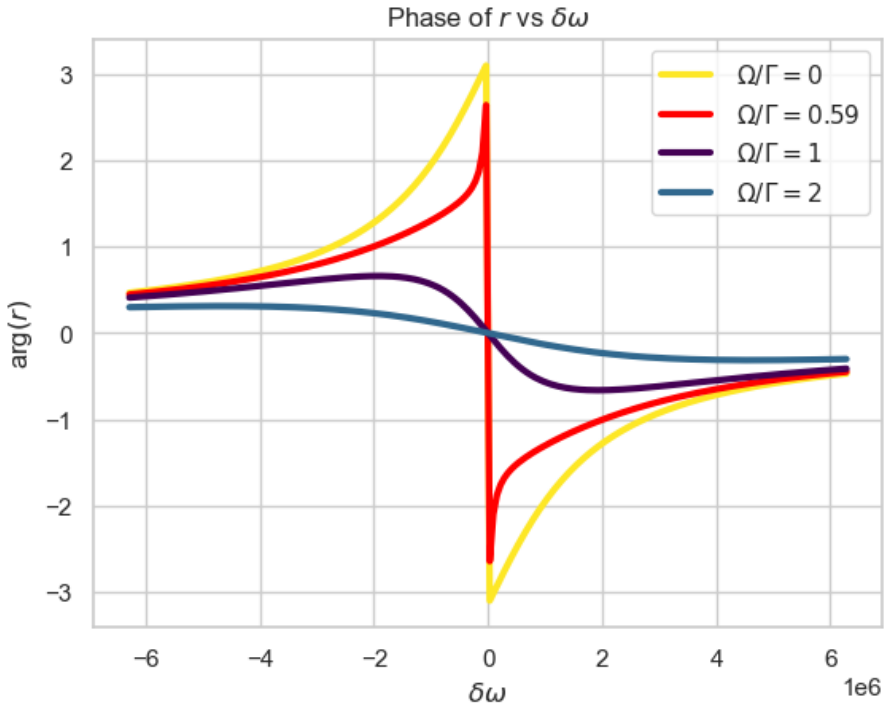

Figure 2.10: The phase of the reflection $|r|$ as a function of the detuning between the atom and probe frequency at varying probing powers.

2.4.2 Primary Thermometry

Each mode is coupled to a waveguide with some temperature T, usually in the range of 10s of mili-Kelvin. Using a reflection measurement it is also possible to measure the temperature of the environment of a qubit, that is the waveguide, as was shown by M. Scigliuzzo et. al in [24]. The reflection of a coherent probing tone on resonance with the qubit can in the low power limit be expressed as

$$r(0) = -1 + \frac{12}{1 + i\Gamma/2\,|\alpha|} n_r + 4\frac{\Gamma_\phi}{\Gamma_r} + 2\frac{\Gamma_{nr}}{\Gamma_r} + \frac{4(\Omega/\Gamma_r)^2}{1 + i\Gamma_r/\,|\alpha|}. \tag{2.66}$$

Where α is the anharmonicity of the mode and n_r the thermal occupancy in the waveguide. From the thermal occupancy it is possible to extract the temperature of the waveguide as $T = \hbar\omega/(k_b \log(1/n_R + 1))$ by assuming a that the photons in the waveguide follow a Bose-Einstein distribution.

2.5 Quantum thermodynamics

2.5.1 Heat flows in quantum systems

In a classical environment the flow of heat between is well described by Fouriers law of heat conductivity

$$J = -k\nabla T, \tag{2.67}$$

formulated by Joseph Fourier in the 1800s [25]. In a quantum environment, Fourier's law does not hold as the currents are caused by stochastic quantum jumps between states. However, in analogue to the classical equation it is possible to define heat currents in quantum systems. By considering the Hamiltonian of a system in contact with multiple reservoirs:

$$\mathcal{H}_{tot} = \mathcal{H}_S + \sum_\alpha \mathcal{H}_\alpha + \mathcal{V}_\alpha, \tag{2.68}$$

where $\mathcal{H}_\alpha$ and $\mathcal{V}_\alpha$ are independent of time with $\mathcal{V}_\alpha$ describing how the system and reservoir interact. Each reservoir has some temperature T_α and chemical potential μ_α.

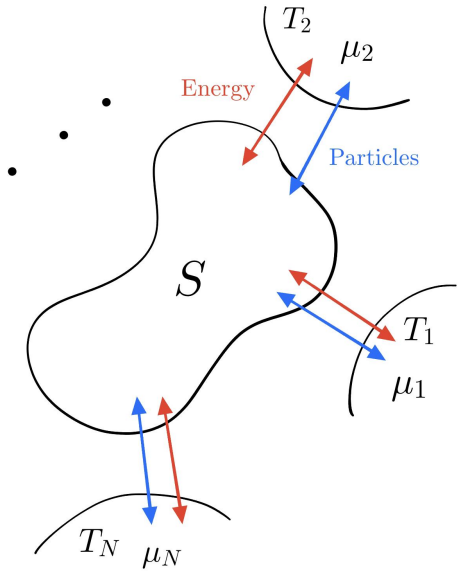

Figure 2.11: A system coupled to a set of reservoirs. The system can exchange particles and energy with each reservoir. Figure taken from [26].

The state of this system is given by a density matrix ρ_{tot} which is assumed to be of the form

$$\rho_{tot} = \rho_s \otimes_\alpha \rho_\alpha \tag{2.69}$$

such that the system state of the system is independent of the state of the reservoirs at time $t = 0$. In analogy to a classical system a heat current to a reservoir can be defined as

$$\partial_t \langle \mathcal{H}_\alpha \rangle = \mathrm{Tr}\{H_\alpha \, \partial_t \rho_{tot}\} = \partial_t \langle \mathcal{H}_\alpha - \mu_\alpha N_\alpha \rangle + \mu_\alpha \langle N_\alpha \rangle = J_\alpha + P_\alpha. \tag{2.70}$$

J_α represents the heat current going in to the reservoir, N_α is the number operator and P_α the power that enters the reservoir [26]. Since the reservoirs considered within the scope of this project are bosonic and occupied only by non-interacting photons the chemical potential vanishes and we find that

$$J_\alpha = \partial_t \langle \mathcal{H}_\alpha \rangle = \mathrm{Tr}\left\{\mathcal{H}_\alpha \mathcal{L}_\alpha \rho_{tot}\right\}. \tag{2.71}$$

With $\mathcal{L}_\alpha$ being the Liouvillian of the bath that the current is flowing in to which describes how the system and bath interact. With this notion of a heat flow it is also possible to recover the first law of thermodynamics for a quantum system. The first law states that the change of energy in a system is given by the change in heat of the system (Q), minus the work done by the system (W)

$$\Delta U = Q - W. \tag{2.72}$$

By considering the time derivative of the total Hamiltonian of the system $\partial_t \langle \mathcal{H}_{tot}(t) \rangle$ we find that

$$\partial_t \langle H_{tot}(t) \rangle = \partial_t \langle \mathcal{H}_s(t) \rangle + \partial_t \sum_\alpha \langle \mathcal{H}_\alpha \rangle + \partial_t \sum_\alpha \langle V_\alpha \rangle \rightarrow \tag{2.73}$$

$$\partial_t \langle \mathcal{H}_s(t) \rangle = P_s(t) - \sum_\alpha (J_\alpha(t) + P_\alpha(t)) - \partial_t \sum_\alpha \langle V_\alpha \rangle$$

which is an equivalent way of expressing the first law of dynamics.

2.6 Thermodynamic uncertainty relations

The second law of thermodynamics states that the entropy produced in a thermodynamic process is always larger than 0. Mathematically this is ensured by the Clausius relation [26]

$$d\Sigma = dS + \sum_{\alpha} \frac{dQ_{\alpha}}{T_{\alpha}} \geq 0. \tag{2.74}$$

It simply states that the total entropy production $d\Sigma$ of any process for a system in contact with thermal reservoirs is larger than 0. dS is is the entropy production in the system and$\frac{dQ_{\alpha}}{T_{\alpha}}$ is of the entropy produced in each reservoir. This can be interpreted as the most fundamental resource of any thermal process, be it an engine or a refrigerator, is the entropy, as it is not possible to reduce the entropy in a closed system. From the laws of thermodynamics it is possible to derive a so called Thermodynamic uncertainty relations (TUR) of stochastic currents [27, 28]. TURs quantify how the signal-to-noise ratio of an observable is bounded by the dissipation needed to generate the signal. They can also be considered inequalites that provide a bound on the precision in a current and the associated thermodynamic cost [[29], [26]], that is the entropy produced in the process. One way of expressing a TUR inequality is as

$$\frac{\sigma}{k_b} \frac{\langle\langle I \rangle\rangle}{\langle I \rangle^2} \geq 2. \tag{2.75}$$

Where σ is the entropy production rate associated with the process and $\langle\langle I \rangle\rangle$ and $\langle I \rangle$ are the variance and mean of a stochastic current. The current I can virtually any kind of current. A current of particles, heat current or even spin currents. The current considered in within the scope of this thesis is a current of photons, equivalent to a heat current. When considering a heat current in the long time limit, it can instead be expressed as

$$\frac{\sigma}{k_b} \frac{D}{J^2} \geq 2, \tag{2.76}$$

where J is a heat current and D its diffusion coefficient. In classical systems fluctuations are present but in the thermodynamic limit the mean is usually much larger than the variance of a current in accordance with the central limit theorem. In quantum systems however this is not the case. In quantum systems currents are an effect of the stochastic nature of the transitions between states [28], mediated by stochastic jump operators We consider the two limits of a TUR. If we have an infinitely precise current in which there are no fluctuations, that is $\frac{\langle\langle I \rangle\rangle}{\langle I \rangle} \to 0$, the entropy produced in the process tends towards infinity as the product of the two is bounded from below by 2. In the same manner we consider a process where no entropy is produced. In this limit the precision tends toward infinity such that $\frac{\langle\langle I \rangle\rangle}{\langle I \rangle} \to \infty$. This can be interpreted as that a TUR provides us with a fundamental trade-off relation between the entropy produced in a process and the amount of noise in the current I.

However it has in recent years been show that it is possible to surpass the lower bound of this inequality in quantum systems. This could be due to the presence of coherence and entanglement [7]. The system considered by Kalaee, Wacker and

Potts in [6] is a Scovil & Schulz-DuBois (SSDB) three-level maser. They show that under the assumption of a Markovian time evolution governed by a Lindblad master equation the SSDB engine can violate the classical TUR inequality. Indicating the possibility of realising quantum machines that experience an advantage to their classical counterpart. The system investigated in this is a Delta system consisting of two strongly coupled qubits, each coupled to a transmission line.

2.6.1 Delta system

In this project we wish to realise a system that resembles the Δ-system discussed in [6].

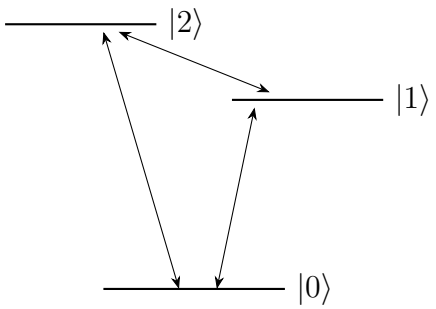

Figure 2.12: Illustration of energy levels and allowed transitions of an ideal delta system.

The system we use to investigate such a system consists of two strongly coupled qubits, described by the Hamiltonian

$$\mathcal{H} = \sum_{i=1,2} \omega_i \sigma_i^+ \sigma_i + g(\sigma_1^+ \sigma_2 + \sigma_2^+ \sigma_1) \tag{2.77}$$

In the symmetric/anti-symmetric basis and a frame rotating at ω_d the Hamiltonian is given by

$$\mathcal{H} = (\omega_A - \omega_d)\sigma_A^+ \sigma_A + \omega_S \sigma_S^+ \sigma_S. \tag{2.78}$$

Where the transformation operator is $U_r = \exp\left[i\omega_d(\sigma_A^+\sigma_A)t\right]$. To this system a coherently driven field is added that couples only to the anti-symmetric mode, driven at frequency $\omega_d = \omega_A$. This enters as a term $\mathcal{H}_d = \frac{\Omega_A}{2}(\sigma_A + \sigma_A^+)$ into the Hamiltonian, where Ω_A represents the Rabi driving strength of the coherent field. The total Hamiltonian is then given by

$$\mathcal{H} = \omega_S \sigma_S^+ \sigma_S + \frac{\Omega_A}{2}(\sigma_A^+ + \sigma_A). \tag{2.79}$$

To allow for transfer of photons between the symmetric and anti-symmetric modes a source of noise is introduced to the system that mediates population transfer between the two modes $|A\rangle, |S\rangle$. This is achieved by introducing a thermal bath that couples to the σ_z operator of one of the bare modes, centered at $\omega = \omega_S - \omega_A = 2g$, effectively bridging the energy gap between the two modes. This affects the time evolution of

the system in the form an additional dissipator that couples to the σ_1^z channel with a rate Γ_ϕ. Expressed in the symmetric/anti-symmetric basis

$$\sigma_1^z = \frac{1}{2}(\sigma_A^z + \sigma_S^z) + \sigma_A^+\sigma_S + \sigma_S^+\sigma_A. \tag{2.80}$$

As the nosie is centered around $2g$ the first term can be disregarded. The operator entering the Liouvillian describing this interaction is then given by

$$O = \Gamma_\phi(\sigma_1^z - \sigma_2^z) = \frac{\Gamma_\phi}{2}(\sigma_A^+\sigma_S + \sigma_S^+\sigma_A). \tag{2.81}$$

With the associated transition rate $\Gamma_\phi/2$, representing the rate at which photons are exchanged between the symmetric/anti symmetric modes. Only considering the first two excited states $|A\rangle, |S\rangle$ and disregarding the higher excitations the thermal process taking place in the system is visualised in figure 2.13.

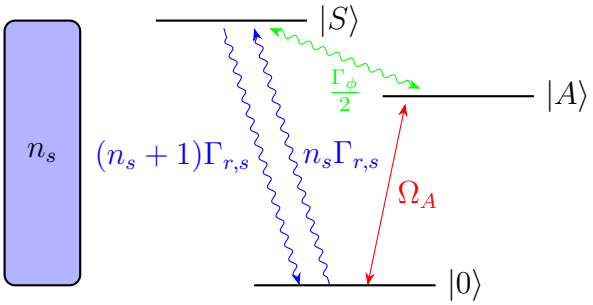

Figure 2.13: Illustration of energy levels and driven transitions of the system and the thermal environment it is coupled to with occupation n_s. The spontaneous emission from the symmetric state to the ground state and absorption is shown in blue. Shown in red is the coherent field driving the $|0\rangle \rightarrow |A\rangle$ transition and in green is the dephasing noise mediating the population transfer back and forth between the two modes.

The process is as follows: The anti-symmetric mode is coherently driven to its excited state, from which a population exchange between the two modes $|A\rangle, |S\rangle$ is incoherently driven, mediated by the dephasing noise that couples to the $\sigma_{z,i}$ channel of one mode. Spontaneous emission from the symmetric state to the symmetric waveguide is monitored and the first two statistical moments are measured. The Lindblad master equation describing the process is given by

$$\dot{\rho} = -i[\mathcal{H}, \rho] + n_s\Gamma_{r,s}\mathcal{D}[\sigma_S^+]\rho + (n_s+1)\Gamma_{r,s}\mathcal{D}[\sigma_S^-]\rho + \frac{\Gamma_\phi}{2}\mathcal{D}[O]\rho. \tag{2.82}$$

2.7 Full counting statistics

In order to extract the statistical moments required to calculate the TUR ratio we employ Full counting statistics (FCS). FCS provides a framework for extracting any statistical moment of a current of particles by providing a method of calculating

how many times particles are exchanged between a system and the reservoirs it is coupled to. For an in depth review of FCS in quantum thermodynamics [27] is recommended. Here, only the methods employed within the scope of this thesis are briefly touched upon and described.
When considering a current in a quantum system, the quantity of interest is how many times a quantum jump has occurred. That is, how many times has the the system transitioned from one state to another through some jump operator being applied to the density operator. In the case of this project, we are interested acquiring the statistics of the photon emission from a superconducting qubit, i.e how many times did a transition from an excited state to the ground state take place, and what is the variance of this current. Each jump is associated with a weight ν_k. and two "opposite" jumps, such as $|0\rangle \to |S\rangle$ and $|S\rangle \to |0\rangle$ have opposite weights such that only the net current is calculated.

To analytically find the moments of a current using FCS, we consider the Liouvillian $\mathcal{L}$ and Hamiltonian $\mathcal{H}$ governing the time evolution of the system, and the net charge $N(t)$ describing how many quantum jumps that have occurred. $N(t)$ can take any value in the set $\mathcal{N}$. To calculate the moments of $N(t)$ we seek the probability distribution $P(n,t) = P(N(t) = n)$. As if $P(t)$ is known it is simple to calculate the current and diffusion coefficient associated with $N(t)$ as $J = \frac{d\mathrm{E}(N(t))}{dt}$ and $D = \frac{d\mathrm{Var}(N(t))}{dt}$ [27].
The state of the system is as usual described by a density matrix ρ that contains all available information about the state of the system. As a mean to find the distribution $P(n,t)$ the n-resolved density matrix $\rho_n(t)$ is defined. Where $\rho_n(t)$ holds the information about the system where n jumps have occurred and the full density matrix can be regained as $\rho = \sum_n \rho_n(t)$. The n-resolved density matrix evolves in accordance with the Lindblad master equation, and for a small step dt the state of $\rho_n(t+dt)$ is given by the Kraus decomposition:

$$\rho_n(t+dt) = M_0 \rho_n(t) M_0^\dagger + \sum_{k=1}^{r} M_k \rho_{n-\nu_k}(t) M_k^\dagger. \tag{2.83}$$

Where the kraus operators M_k corresponding to the different channels in which quantum jumps can occur and M_0 represents no jump happening in the time step dt. The Kraus operators are related to the Lindblad jump operators by

$$M_k = \sqrt{dt} L_k \tag{2.84}$$

$$M_0 = I - i\left(\mathcal{H} - \frac{i}{2}\sum_k L_k^\dagger L_k\right) dt \tag{2.85}$$

where a normalisation condition of the Kraus operators is given by

$$M_0^\dagger M_0 + \sum_k M_k^\dagger M_k = 1 + \mathcal{O}(2). \tag{2.86}$$

as we consider only the possibility of a single jump happening in a time step. By rewriting ρ in terms of its Fourier series with coefficient χ

$$\rho_\chi(t) = \sum_n e^{in\chi} \rho_n(t) \tag{2.87}$$

and fourier transforming equation 2.83 it takes the following form:

$$\frac{d\rho_\chi(t)}{dt} = \mathcal{L}_\chi \rho_\chi(t). \tag{2.88}$$

Where χ is the counting field and $\mathcal{L}_\chi$ is referred to as the tilted Liouvillian given by

$$\mathcal{L}_\chi \rho = -i[\mathcal{H}, \rho] + \sum_k \left(e^{i\chi\nu_k} \mathcal{L}_k \rho \mathcal{L}_k^\dagger - \frac{1}{2} \left\{ L_k^\dagger L_k, \rho \right\} \right). \tag{2.89}$$

Equation 2.88 has the same form as that of a general quantum master equation. Formally the solution of that equation is given by $\rho_\chi(t) = e^{\mathcal{L}_\chi t}\rho_0$ from which the probability distribution $P(n,t)$ is recovered as

$$P(n,t) = \int_{-\infty}^{\infty} \frac{d\chi}{2\pi} e^{in\chi} \mathrm{tr}\{\rho_\chi(t)\}. \tag{2.90}$$

The Fourier transform of a probability distribution is know as the characteristic function $M(\chi,t)$ of the probability distribution, in equation 2.90 given by $\mathrm{tr}\{\rho_\chi(t)\}$. From the characterist function of a probability distribution $P(n,t)$ all moments of $N(t)$ can be calculated as

$$\langle\langle N(t)^i \rangle\rangle = (-i\partial_\chi)^i C(\chi,t) = (-i\partial_\chi)^i \ln(M(\chi,t)) \tag{2.91}$$

evaluated at $\chi = 0$. Going in to the long time limit the cumulant generating function can be approximated as $C(\chi,t) \approx \lambda_0(\chi)t$ where $\lambda_0(\chi)$ represents the largest eigenvalue of the tilted Liouvillian. The scaled cumulant generating function can then be defined as $C(\chi) = \lim_{t\to\infty} \lambda_0(\chi)$. So the problem of finding the mean and variance reduces to finding the largest eigenvalue of the tilted Liouvillian. Resulting in

$$J = -i\partial_\chi C(\chi) \mid_{\chi=0} \tag{2.92}$$

and

$$D = -\partial_\chi^2 C(\chi) \mid_{\chi=0} . \tag{2.93}$$

2.8 Measuring the mean and variance of a photon current

In this section, the theoretical background for measuring the variance and mean value of a photon current using input-output theory is presented. The assumptions and limitations of the technique are presented and discussed. The derivation was done by Dr. Mark T. Mitchison of Trinity College Dublin.

Like in section 2.4, we consider the input and output field of a wave guide. $b_{i/o}(t)$ corresponds to the input/output field of the wave guide and L is the system operator to which the wave guide is coupled. In the case of a transmon coupled to a wave guide, $L = \sqrt{\kappa}a$. The output is then equal to

$$b_o(t) = b_i(t) + L, \tag{2.94}$$

Where the Canonical commutation relations are imposed on b so that

$$[b_{i/o}(t), b^{\dagger}_{i/o}(t')] = \delta_{i,o}(t - t') \tag{2.95}$$

and

$$[b_{i/o}(t), b_{i/o}(t')] = 0. \tag{2.96}$$

And the input field is assumed to be in a vacuum state such that $\langle b_i^{\dagger}(t) b_i(t) \rangle = 0$, where $\langle \cdot \rangle$ represents the ensemble average of the operator. The signal at the output of a chain of linear amplifiers with added noise is defined as:.

$$S'(t) = \sqrt{G} b_o(t) + \sqrt{G-1} h^{\dagger}. \tag{2.97}$$

h reperesent a bosonic noise field corresponding to white noise added by the amplification chain. It follows that $[h(t), h^{\dagger}(t')] = \delta(t - t')$ and $[h(t), h(t')] = 0$. The signal is rescaled as $S(t) = S'(t)/G$ and we go in the large limit of G.

$$S(t) = b_o(t) + \sqrt{\frac{G-1}{G}} h^{\dagger}(t) \to b_o(t) + h^{\dagger}(t), \tag{2.98}$$

This is a good assumption as the amplification of a readout line typically ranges between 80-100dB. The added noise by the amplification chain is assumed to be Gassuian and equal to the number of thermal photons n in the readout line, such that

$$\langle h^{\dagger}(t) h(t') \rangle = n \delta(t - t'). \tag{2.99}$$

Finally, to account for divergences a exponential response function is defined such that

$$\tilde{S(t)} = \int_0^t f(t - t') S(t'). \tag{2.100}$$

Where the response function is normalised

$$\int_0^{\infty} dt f(t) = 1 \tag{2.101}$$

and is assumed to have a response time much shorter than the integration time. This allows us to define the response function as

$$f(t) = 2\Lambda e^{-2\Lambda t}, \tag{2.102}$$

where Λ represents the detection bandwidth of the measurement apparatus.
We now wish to calculate the energy associated with the signal field $\tilde{S}$. We calculate the integrated current

$$Q = \int_0^T \tilde{S}^{\dagger}(t) \tilde{S(t)}, \tag{2.103}$$

and its ensemble averages $\langle Q \rangle$, where Q is a dimensionless quantity representing the number of detected jumps during the integration time.

$$\langle Q \rangle = \int_0^T \int_0^t dt_1 \int_0^t dt_2 f^*(t - t_1) f(t - t_2) \langle L^{\dagger}(t_1) L(t_2) \rangle + (1+n) \int_0^T dt \int_0^t dt_1 \, |f(t - t_1)|^2 \tag{2.104}$$

The first-order correlation function is given by

$$g^{(1)}(t,t') = \int_0^t dt_1 \int_0^{t'} dt_2 \frac{\langle L^\dagger(t_1)L(t_2)\rangle}{\langle L^\dagger L\rangle}. \tag{2.105}$$

In analogy to this the "smoothed correlation function" is defined as

$$\tilde{g}^{(1)}(t,t') = \int_0^t dt_1 \int_0^{t'} dt_2 f^*(t-t_1)f(t'-t_2)\frac{\langle L^\dagger(t_1)L(t_2)\rangle}{\langle L^\dagger L\rangle}. \tag{2.106}$$

and a function λ which corresponds to the measured noise during a measurement is defined as

$$\lambda(t) = \int_0^t dt_1 \left|f(t_1)\right|^2. \tag{2.107}$$

By going in the long time limit, where the measurement time is much longer than the the typical decay rate of the sample we have

$$\lambda(t) \to \int_0^\infty dt \left|f(t)\right|^2 = \Lambda \tag{2.108}$$

where it holds true that $\int_0^\infty dt f(t) = 1$ in accordance with equation 2.101. Under these assumptions we find that the integrated current is equal to

$$\langle Q\rangle = \int_0^T \left(J\tilde{g}^{(1)}(t,t) + (1+n)\lambda(t)\right) \to \frac{\langle Q\rangle}{T} = J + \frac{\Lambda}{\eta} \tag{2.109}$$

where due to the long time limit the correlation function only depends on the time difference $t-t'$, $\tilde{g}^{(1)}(t,t') \approx g^{(1)}(t-t')$ and η is the measurement efficiency of the readout apparatus defined as $\eta = \frac{1}{n+1}$.
So by measuring Q in an alternating fashion where the process of interest is being driven and where only the background is being measure the current J can be extracted as

$$\langle Q_{on}\rangle - \langle Q_{off}\rangle = J + \frac{\Lambda}{\eta} - \frac{\Lambda}{\eta} = J. \tag{2.110}$$

In a similar fashion the diffusion coefficient can be extracted by measuring the second moment of the integrated current $\langle Q^2\rangle$. By applying wicks theorem to the Gaussian noise operator it's found that

$$\langle h(t_1)h(t_2)h^\dagger(t_3)h^\dagger(t_4)\rangle = (1+n^2)\left(\delta(t_1-t_3)\delta(t_2-t_4) + \delta(t_1-t_4)\delta(t_2-t_3)\right) \tag{2.111}$$

resulting in

$$\begin{aligned}\langle Q^2\rangle &= 2\int_0^T dt \int_0^t dt' \langle \tilde{S}^\dagger(t')\tilde{S}^\dagger(t)\tilde{S}(t)\tilde{S}(t')\rangle \\ &= 2\int_0^T dt \int_0^t dt' \Big[J^2\tilde{g}^{(2)}(t,t') + \eta^{-2}\lambda(t)\lambda(t') + \eta^{-2}|\Delta(t,t')|^2 \\ &+ J\eta^{-1}\lambda(t)\tilde{g}^{(1)}(t',t') + J\eta^{-1}\lambda(t')\tilde{g}^{(1)}(t,t) + 2J\eta^{-1}\mathrm{Re}\left(\Delta(t,t')\tilde{g}^{(1)}(t',t)\right)\Big].\end{aligned} \tag{2.112}$$

where $\tilde{g}^2(t,t')$ is the smoothed second order coherence function

$$\int_0^{t'} dt_1 \int_0^t dt_2 \int_0^t dt_3 \int_0^{t'} dt_4 f^*(t'-t_1) f^*(t-t_2) f(t-t_3) f(t'-t_4) \frac{\langle L^\dagger(t_1) L^\dagger(t_2) L(t_3) L(t_4)\rangle}{\langle L^\dagger L\rangle} \tag{2.113}$$

and $\Delta(t,t') = \int_0^{\min(t,t')} f^*(t-t_1) f(t'-t_1)$. Using the definition of $\lambda(t)$ as in equation 2.107 and as when measuring the first moment we once again assume a long integration time such that $\tilde{g}^{(2)}(t,t') \to \tilde{g}^{(2)}(t-t')$. This yields

$$\frac{\mathrm{Var}(Q)}{T} = \frac{\Lambda}{2\eta^2} + \frac{2J}{\eta} + \frac{2J^2}{T} \int_0^T dt \int_0^t dt' \left[\tilde{g}^2(t-t') - 1\right]. \tag{2.114}$$

Where the diffusion constant D is defined as [27]

$$D = J + 2J^2 \int_0^\infty d\tau \left[g^{(2)}(\tau) - 1\right]. \tag{2.115}$$

We calculate the diffision coefficient D as

$$D = \frac{1}{T}(\mathrm{Var}(Q_{\mathrm{on}}) - \mathrm{Var}(Q_{\mathrm{off}})) - \frac{2-\eta}{\eta} J. \tag{2.116}$$

Equipped with the necessary tools to measure fluctuations in a quantum system we now move to the methods employed in this project.

3

Experimental methods

Equipped with the necessary theory we now present the methods applied in this project. The experimental setup and methods employed are explained in detail. The device used was designed by Aamir Ali and is the same as was used in [30]. It was fabricated by Claudia Castillo-Moreno at mu-labs, Chalmers. The measurements are performed using Keysight Labber, a software for communicating with instruments using different communication protocols.

3.1 The dilution refrigerator

For realising quantum computing it's important to mitigate the environments impact on the state of the qubit. For superconducting qubits this done by working in an environment where the temperature is much lower than the typical qubit energy. That is $\hbar\omega \gg k_b T$. When using superconducting circuits, the platform that the experiments are performed in is a dilution refrigerator. Dilution refrigerators operate at temperatures close to absolute zero, with state of the art fridges reaching temperatures around $\sim$ 10mK. This is achieved by having a mixture of two helium isotopes, ^{3}He and ^{4}He as the working medium where the low atom-atom bond of ^{3}He enables cooling to sub 1K levels . The fridge is designed to have different stages at different temperatures (figure 3.1).

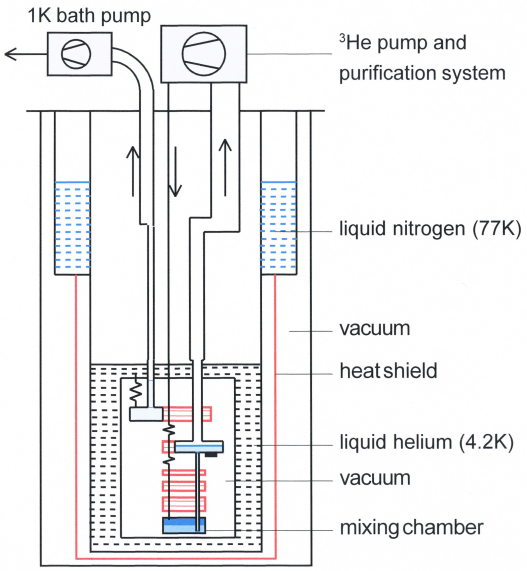

Figure 3.1: Schematic image showcasing how a dilution refrigerator operates. The image is taken from [31].

The different temperature stages in the dilution refrigerator play an important role in cooling down the system to the desired temperatures needed for quantum computing experiments with superconducting circuits. Typically, each stage include a series of thermal and magnetic shields, built to reduce the temperature progressively from room temperature to the milikelvin range. As the system reaches temperatures below 1 K, the cooling is performed by mixing ^{3}He into ^{4}He. This process occurs in the mixing chamber, where ^{3}He atoms dilute into ^{4}He, absorbing heat in the process and enabling that stage to reach temperatures below 10mK.
The mixing chamber is where the qubits are usually mounted. In this stage the effect of thermal noise is minimized, thus reducing the effect of the environment on the qubits and increasing the coherence times. The low thermal background makes it possible maintaining quantum states over the time scales necessary for quantum computation.
In summary, the dilution refrigerator is a key enabling technology for superconducting qubits, providing the ultra-low temperature environment necessary for controlling quantum systems.

3.2 experimental setup

In this section the experimental setup used for the measurements in this project is presented. The room temperature devices used to control the sample and collect data is also described.

The sample is mounted in the lowest chamber of a dilution refrigerator where the temperature typically is $\sim$ 10mK. Between the room temperature electronics used and the sample are a series of filters, attenuators and other standard microwave

components that alter the signals so that they are at appropriate energy scales when they reach the sample.

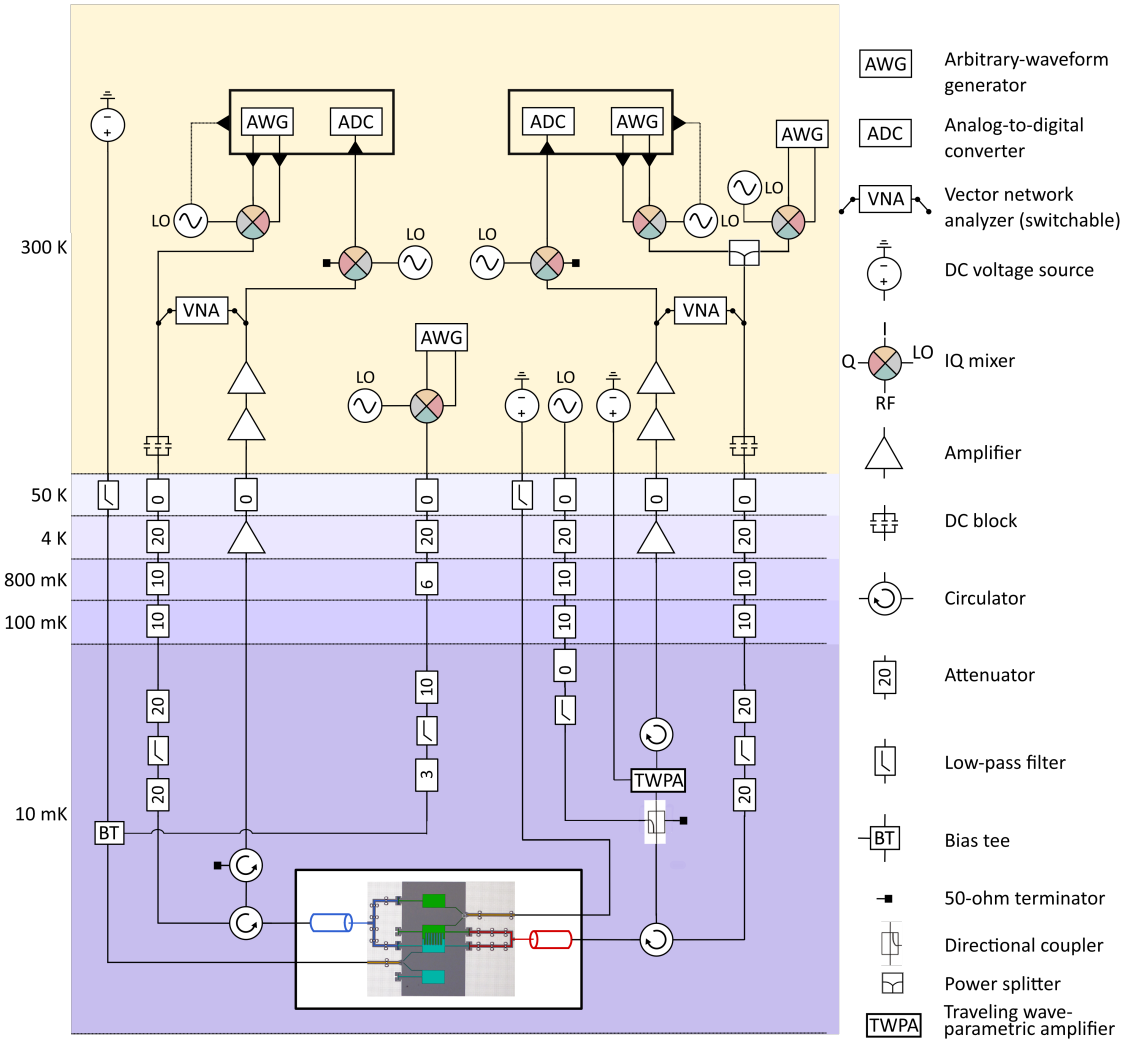

Figure 3.2: Simplified experimental setup. The different colors in the background indicate the temperature of each stage in the setup. The characterisation of the system is perfromed using the VNA coupled to the each of the waveguides input/output line. The main measurements are performed using the AWG and ADC inside the black boxes at the top of the figure. This instrument is the Quantum Machines OPX+ which allows us to perform rapid calculations mid measurement using a built in Field Programmable Gate Array (FPGA).

The sample installed in the fridge, shown at the bottom of image 3.2 is the same as was used by Sundelin in [30]. It is a symmetry selective device that operates in such a way that each of the wave guides couples strongly to only one of the modes. The details of this interaction can be read about in [32].

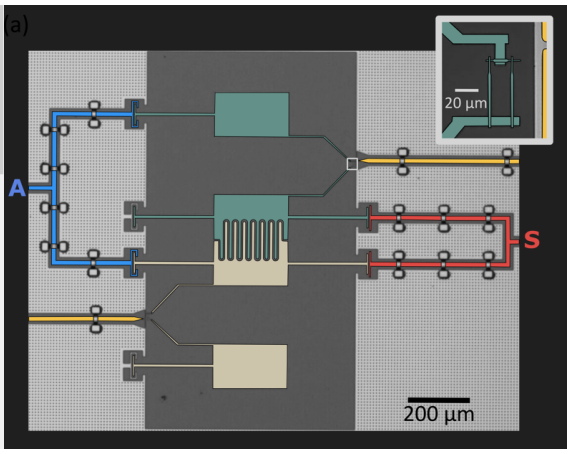

Figure 3.3: False color image of the symmetry selective device. In red is is the symmetric wave guide that couples strongly to the symmetric mode and in blue the anti-symmetric wave guide that couples strongly to the anti-symmetric mode. The yellow transmission lines are the flux lines, one of which is populated with the dephasing noise. Inset: a squids that introduces the non linearity in the circuit and allows for flux tuning of the device. Image taken from [30].

3.3 Characterization of the system

Before performing the main measurements of the project, the device under test is characterized. This includes finding the qubits, determining the working point of the system with respect to the external flux sources, and calibrating the traveling wave parametric amplifier.

3.3.1 Reflection Spectroscopy

Using a VNA wired as shown in figure 3.2 the spectroscopy of the system is started to find the point where the qubits are fully hybridized. That is, the flux point at which the distance between the modes ($\Delta = \omega_S - \omega_A$) is minimized. The system is characterised by performing a reflection measurements over a large frequency span, while measuring the reflection (S_{11}) off of the qubit while varying the power of the probing tone. Once both qubits have been found where no external flux is applied one of the flux sources is fixed at 0.75V while the other voltage source is swept. The mode frequencies at each flux point are extracted as the points of lowest reflection. From this the flux point where the qubits are fully hybridised is extracted as the flux point where the difference in frequency, $\Delta = \omega_S - \omega_A$ is minimised. In figure 3.4 the spectroscopy is shown and in 3.5 the resulting detuning between the modes is plotted.

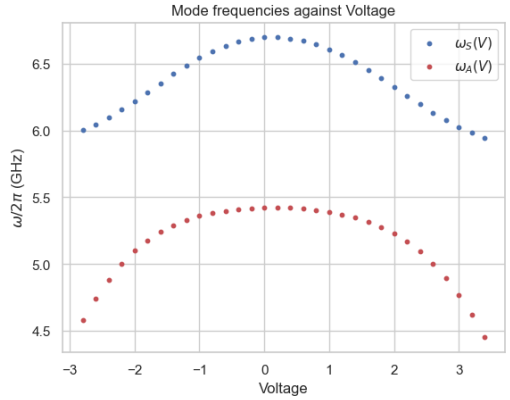

Figure 3.4: Measured mode frequencies from both ASWG and SWG as functions of the voltage applied to the flux line.

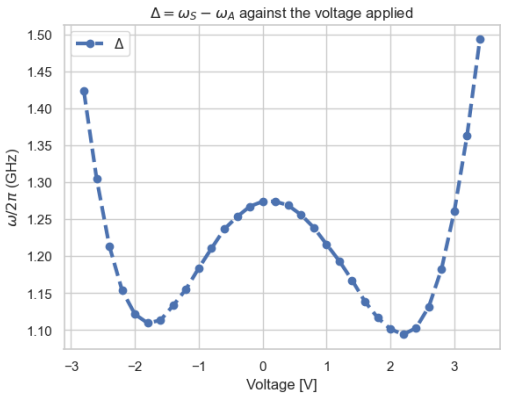

Figure 3.5: The frequency difference $\Delta = \omega_S - \omega_A$ between the two modes as a function of the voltage applied to the flux line.

We find that the modes are fully hybridized at when 2.2 volts are applied to the flux line. At this point we find the coupling strength between the qubits to be $2g \sim$ 1127MHz. To more accurately find the mode exact mode frequencies and coupling rates of each qubit to its respective wave guide and environment, an additional spectroscopy measurement is performed where the power is swept while keeping the flux fixed as described in the results.

3.3.2 IQ mixing

An IQ mixer can be operated as both an up and down converter, allowing us to generate and readout the desired waveforms using the OPX+. It's a three wave mixer allowing us to encode both I (in phase) and Q (out of phase) signals in a converted signal. The output signal has frequency components at frequencies $\omega_{\mathrm{RF}} = \omega_{\mathrm{LO}} \pm \omega_{\mathrm{IF}}$ where the unwanted side band can be removed through calibration of the phase of each quadrature, ϕ_I, ϕ_Q.

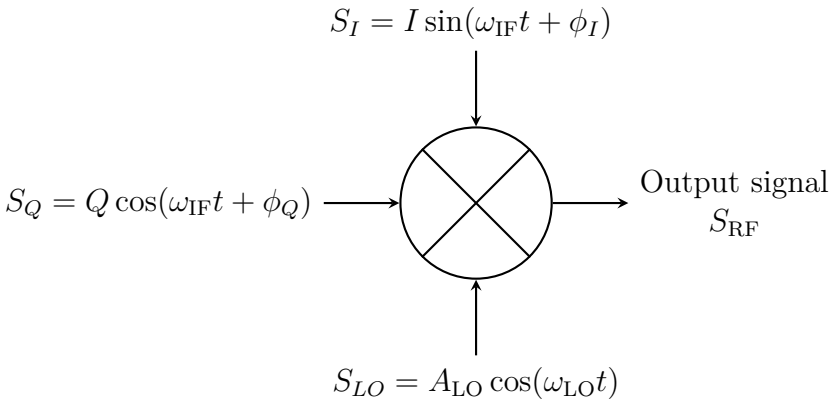

Figure 3.6: Schematic image of an IQ-mixer operated as an up converter.

In a similar manner the IQ-mixer can be used for down conversion, where instead

the output (channel I and Q) will have frequency components $\omega = \omega_{\mathrm{RF}} \pm \omega_{\mathrm{LO}}$.

3.3.3 TWPA calibration

On the readout line for the symmetric mode a traveling wave parametric amplifer (TWPA) is installed. A TWPA is a near quantum limited amplifier, meaning it is, in principle, capable of adding only a half a photon of noise while amplifying the signal. This is a mean of increasing the (SNR), where $\mathrm{SNR} = \frac{P_{\mathrm{signal}}}{P_{\mathrm{noise}}}$. It is important to have a high SNR as many of the measurements performed require many averages and by increasing the SNR the measurement time can be reduced significantly. As seen in the wiring diagram in 3.2 the TWPA is the first amplifier in the amplification chain of the symmetric mode. The importance of having a low noise amplifier as the first amplifier can be understood by considering Friis formula for the noise temperature of a chain of cascaded amplifiers [33].

$$T_{eq} = T_1 + \frac{T_2}{G_1} + \frac{T_3}{G_1 G_2} + ... \tag{3.1}$$

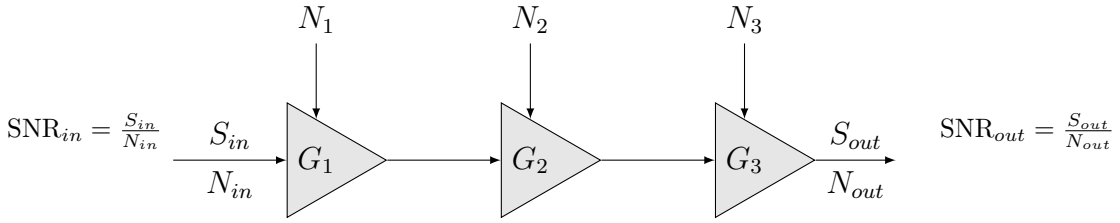

Figure 3.7: Image of 3 cascaded amplifiers. Each amplifier amplifies the signal and noise by a factor G_i while also adding some thermal noise N_i.

Looking at equation 3.1 it is clear that if the first amplifier in the chain has a large gain while also adding few noise photons the noise at the output will be low. This is why the TWPA is the first amplifier in the amplification chain.
The TWPA used in the experiments was fabricated by VTT in Finland. It is a three wave mixing amplifier that can be tuned by a external flux source and a pump signal. As a means to find the optimal working point of the TWPA where the SNR at the output is maximised we measure the gain and coefficient of variation (CV) while varying said parameters. First the flux is swept while having a constant pump power and frequency to find at what flux the gain is of the TWPA is highest. This is done as the flux-bias in theory only should adjust the impedance of the TWPA, thus the points with high gain should correspond to where the the impedance of the TWPA and readout lines impedance are best matched. Next, while having a constant flux the pump power and frequency is swept while sending a strong coherent tone at frequency ω_S through the TWPA. For each point ω_p, Ω_p 100000 measurements are performed where the I and Q component of each measurement is saved. From the saved data a gaussian is fitted to the radial distribution $r = \sqrt{I^2 + Q^2}$ of the

measurement from which the mean μ and standard deviation σ of each probing point is calculated.

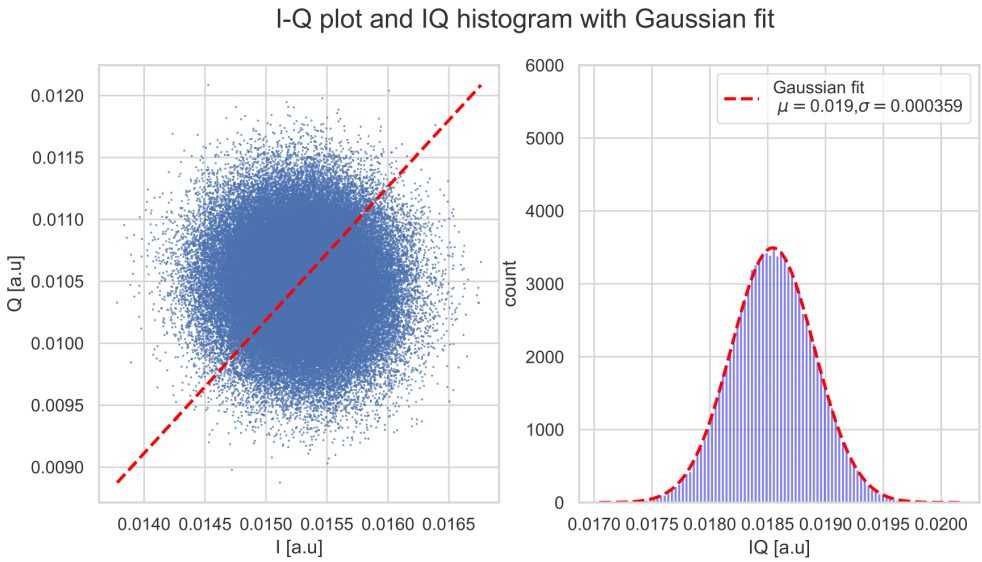

Figure 3.8

This allows us to calculate the CV for each point, where a low value of CV corresponds to a low thermal noise value at the last stage of the amplification chain.

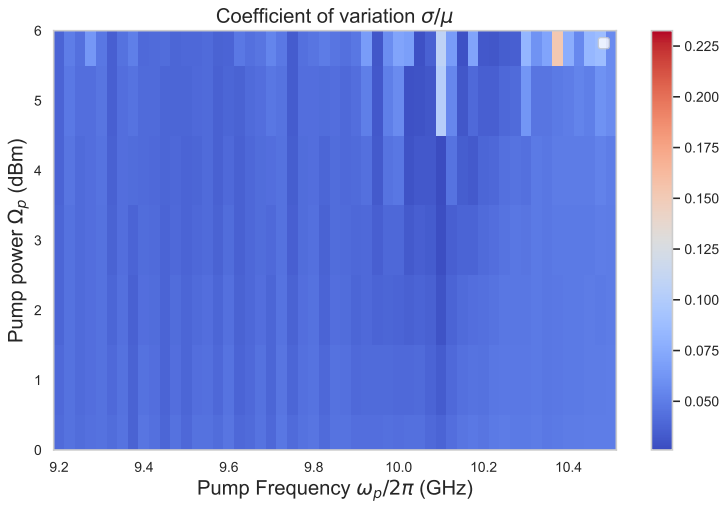

Figure 3.9: Coefficient of variation for varying values of the pump power Ω_P and frequency ω_p.

We find that the CV lowest when the pump has a frequency of $\omega_p/2\pi = 10.1$GHz and power $\Omega_P = 3.5$dBm. Although this method does not quantify the number of thermal photons added by the quantum limited amplifier it gives a good indication as to where the TWPA best operates. To that end a measurement of the Mollow-triplet will be performed to extract the number of thermal photons present in the symmetric waveguide.

3.4 PSD measurements

The power spectral density measurements are performed using a quantum machines OPX+. It's an arbitrary waveform generator (AWG) and analogue-to-digital converter (ADC) on the same system. The sampling rate of the OPX+ is 1GHz, which means that in accordance with Nyqvist sampling theorem it can generate and sample arbitrary waveforms with a frequency of at most 500MHz without the effect of aliasing being visible. As the frequencies of the modes of the system are in the GHz regime we need a way of generating pulses at this frequency. To allow for this the signals from the OPX+, which are limited to be at most 500MHz, are up/down converted using IQ-mixers as shown in figure 3.2.

3.4.1 Mollow triplet calibration

The PSD measurements form the foundation of this thesis, as they provide us with a way of measuring the power emitted from the circuit. But, the signal measured at the digitaliser is not the same as the signal that would be measured at the output of the circuit as the signals have gone through a chain of amplification and digital demodulation. As a means to find the true PSD of a signal, a calibration is performed using the mollow triplet for which a theoretical expression is known. To the measured data equation 2.45 is fitted where only the drive strength Ω and an additional prefactor is fitted to find the gain of the readout line. This measurement is performed on both the symmetric mode and the antisymmetric mode. On the SWG the Mollow triplet is used as a mean to extract the gain of the amplification chain so that future PSD measurement on the SWG can be related to this and the measured signal can scaled to units of Watts. Whereas on the ASWG the quantity of interest is Rabi drive rate that enters the Hamiltonian. To this end, multiple Mollow triplets are measured while the drive strength of the AWG is varied and the Rabi rate is extracted for each measurement.

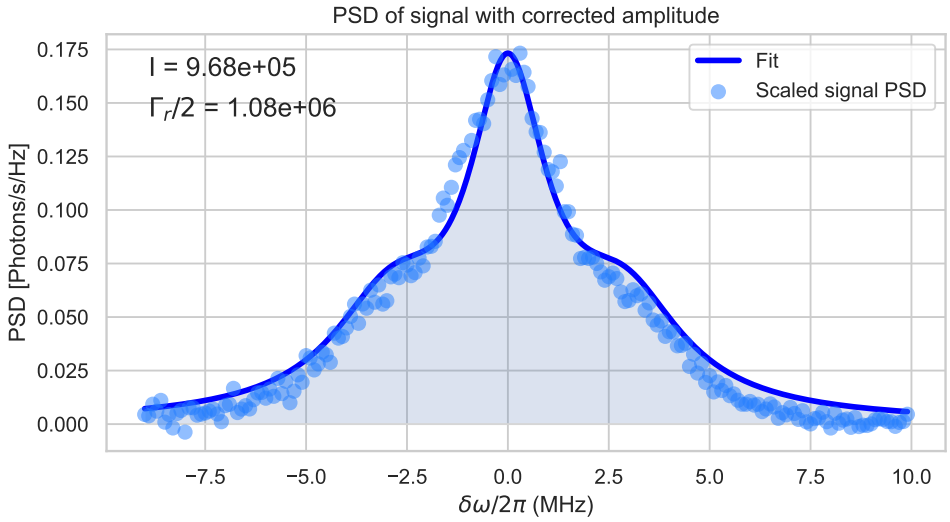

Figure 3.10: Measured Mollow triplet on the SWG and fitted function. The shaded region indicates the integrated current.

We find that the "gain" of the fit is $g_s = 3.0317 \cdot 10^{15}$ and verify that this value is correct by comparing the integral (shaded region in figure 3.10) is equal to $\frac{\Gamma_r}{2}$. The difference between the integral I and $\Gamma_r/2$ is attributed to the finite bandwidth of the measurement. The gain is used as a scaling factor on all future PSD measurements from the SWG. We also find that the number of thermal photons present is $n_{th} = 10.58012468$, resulting in a quantum efficiency $\eta = \frac{1}{1+n_{th}} = 0.09451684$.

3.4.2 Parsevals theorem

In order to reduce the measurement time of the when recording the heat flows and variance measured we use Parsevals theorem. Parsevals theorem states that for two square integrable functions u, v related by a unitary transformation [34]

$$\int_{-\infty}^{\infty} |u(x)|^2 = \int_{-\infty}^{\infty} |v(x)|^2 \,. \tag{3.2}$$

In the case of the PSD measurements performed where we wish to measure the current this means that the current

$$J = g_s \int_{-\infty}^{\infty} d\omega S(\omega) = A \int_{-\infty}^{\infty} dt \, |s(t)|^2 \tag{3.3}$$

where $|s(t)|^2$ is the square of the time trace of the measured signal and $S(\omega)$ its Fourier transform $S(\omega) = |\mathcal{F}\{s(t)\}|^2$. The prefactor A is calculated by performing the same measurement twice. Once using a PSD measurement and once measuring the time trace and relating the two by through A. Thus the task of first calculating the Fourier transform of the time trace and in post processing integrating it reduces to taking the inner product of the time trace with itself. Significantly reducing the computational time of the measurement as no Fourier transforms need to be computed in the measurements.

3.5 Synthesised thermal fields

Both the SWG and the dephasing channels are populated with synthesised thermal fields that are generated using a PXIe AWG. The white noise is generated at an intermediate frequency between $100 - 500$MHz with a bandwidth of 50MHz and up converted using an IQ-mixer and LO as described in section 3.3.2 . The white noise can be considered thermal baths as the they cover a relatively broad band (50MHz) and are unaffected by the state of the system, i.e. the temperature of the baths is unaffected by emission or absorption of photons occurring within the system. The temperature of the thermal field populating the SWG is calculated by performing a PSD measurement while sending in thermal baths and relating the height to that of the Mollow triplet, which corresponds to one thermal photon.

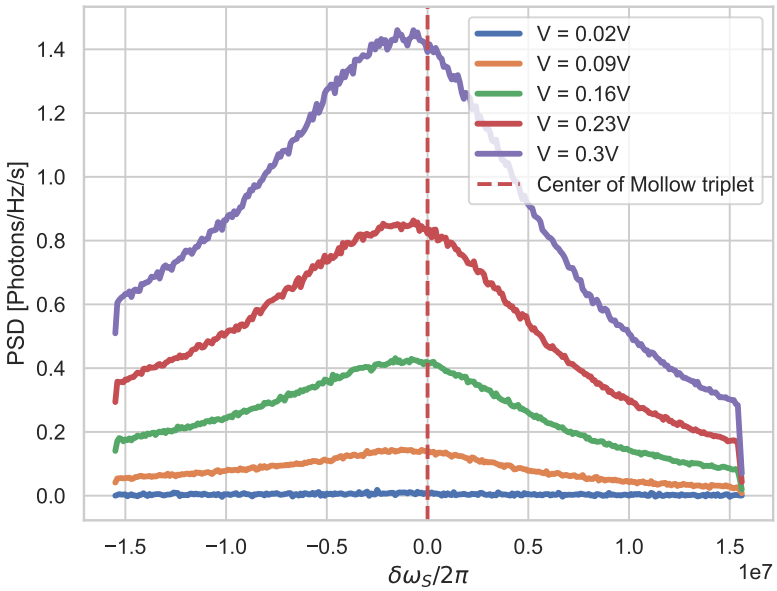

Figure 3.11: Synthesised thermal baths that are populating the SWG at varying voltages. The fields can be considered thermal as their state is uncorrelated with the state of the system (white noise) and its width extends well beyond the line width of the symmetric mode [35].

Altough measured thermal baths in figure 3.11 appear to be normally distributed around ω_s this is not the case. The shape of the measured signal is different from the baths that are generated mainly due to the gain profile in the TWPA but is also modified by the demodulation process taking place in the OPX+. The "peak" close to $\delta\omega_s = 0$ is an effect of the gain profile of the TWPA, which has a significantly higher gain in a narrow region around w_s than elsewhere. In reality the shape of the thermal baths sent to the SWG are square waves centered at ω_s. This was verified by performing the same measurement using a spectrum analyser to measure the output of the AWG. To determine the number of thermal photons the same measurement setup used for the Mollow triplet measurement has to be used to be able to relate the measured value to each other in a sensible way. The number of thermal photons is extracted as the height of the PSD trace of the thermal field where $\delta\omega_S = 0$ and fitted against the a quadratic function, as the power $P \propto V^2$.

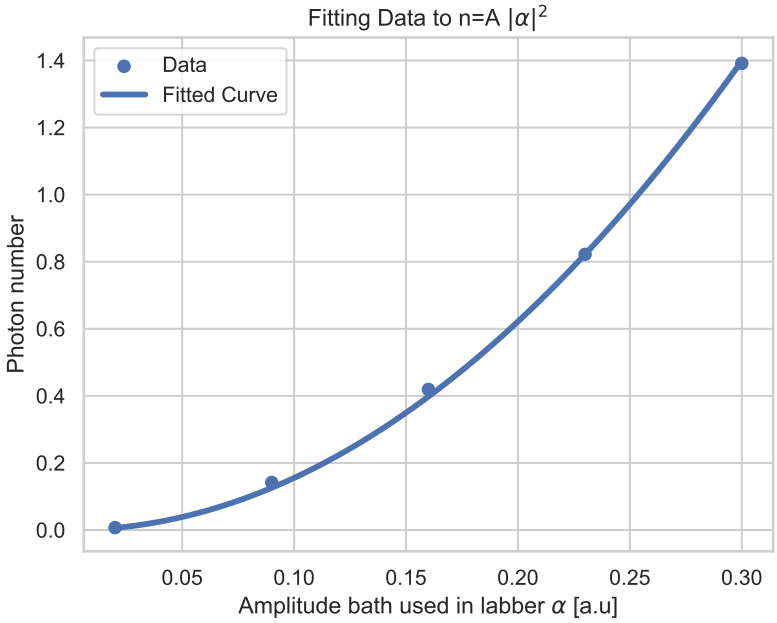

Figure 3.12: Quadratic fit to the temperature of thermal baths populating the SWG.

The temperature of the thermal field, as anticipated, has a quadratic dependence on the applied voltage.

4

Results

In this part the results of the project are presented. We begin by presenting the system characterisation and the parameters found. The calibration of the dephasing noise and pump power is then presented. We then showcase the power transfer between the modes and its dependence on the dephasing noise and coherent drive. Lastly the results of the current fluctuation measurements are presented and compared to simulations using full counting statistics.

4.1 Determining the coupling rates

To find the coupling rates of the qubits to the environment and exact mode frequencies a reflection measurement as described in 2.4.1 is performed on each qubit while varying the probing power to find the magic power at which the qubit is fully saturated. When performing the fit of the reflection the pure dephasing Γ_ϕ is assumed to be 0 as the fit used provides no way of differentiating effects of pure dephasing or non-radiative dephashing Γ_{nr}.

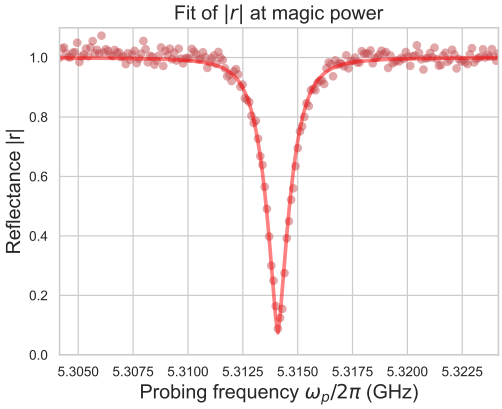

Figure 4.1: Fit to the normalised reflection magnitude off the ASWG at the magic power.

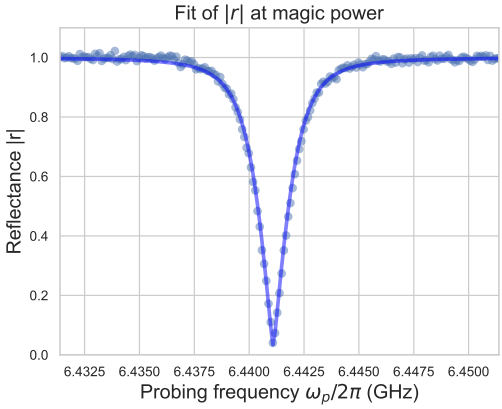

Figure 4.2: Fit to the normalised reflection magnitude off the SWG at the magic power.

As we expected the magnitude of the normalised reflection $\mid r \mid$ is equal to 1 when probing far from the mode and a narrow "dip" is observed at the mode frequency where we are coherently driving the lowest transition. We find excellent agreement between the theory and experimentally measure reflection of each mode. We see that the reflection of both modes nearly completely destructively interacts with the

incoming field at the extracted mode frequencies at their respective magic powers in figures 4.1, 4.2.

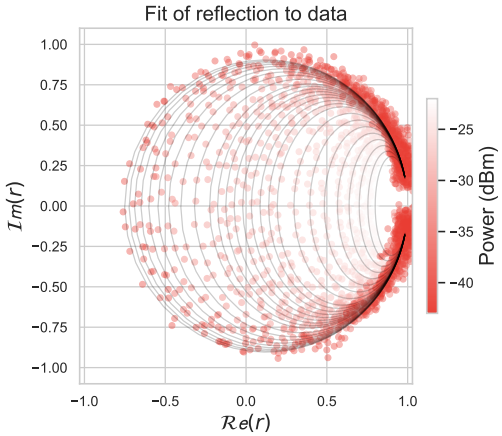

Figure 4.3: Circle fit to ASWG reflection at the varying powers.

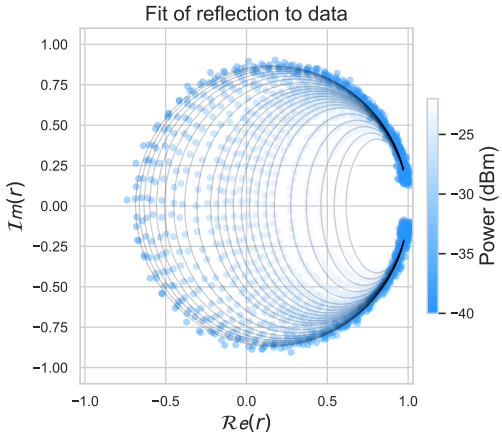

Figure 4.4: Circle fit to SWG reflection at varying powers.

From the figures where complex reflection is shown (figures 4.3 , 4.4) we note that the reflection does a complete phase shift and approaches the unity circle at powers lower than the magic power, as expected. The seemingly better fits to the SWG reflection data is attributed to the TWPA installed on that line. As equation 2.65 is in excellent agreement with the acquired data we can confidently extract the decay rates of each mode. We determine the mode frequencies and coupling rates of each mode, displayed in table 4.1.

	ASWG	**SWG**
$\omega/2\pi$ (GHz)	5.31	6.44
$\Gamma_r/2\pi$ (MHz)	1.84	2.27
$\Gamma_{nr}/2\pi$ (MHz)	0.13	0.27
Γ_r/Γ_{nr}	13.96	8.31

Table 4.1: The extracted mode frequencies and coupling rates of each mode.

We find that the isolation Γ_r/Γ_{nr} of the anti-symmetric mode is close to 14 and 8 for the symmetric mode. Allowing for decent control of each mode using it's strongly coupled waveguide without interfering with the other mode in an undesired way.

4.2 Calibrating the environment

4.2.1 Pump power calibration

We measure the power spectral density of the ASWG while varying the driving strength of the of the pumping tone with frequency ω_a going in to the ASWG. For each power a total of 18 million averages are acquired to which a Mollow triplet is fitted, where the only free parameter is the drive strength Ω and a pre-factor

as the coupling rates are know from the reflection fit of the mode. Before the fits are performed the data is adjusted to account for the coherent tone that would otherwise be visible as a very high peak at ω_a. To this end the single point at $\omega = \omega_a$ is removed from the measurement data. The fitted Mollow triplets are shown in figure 4.5. The drive strength Ω_0 corresponds to the driving strength when the OPX+ pulse amplitude is $0.01\mathrm{V_{pp}}$.

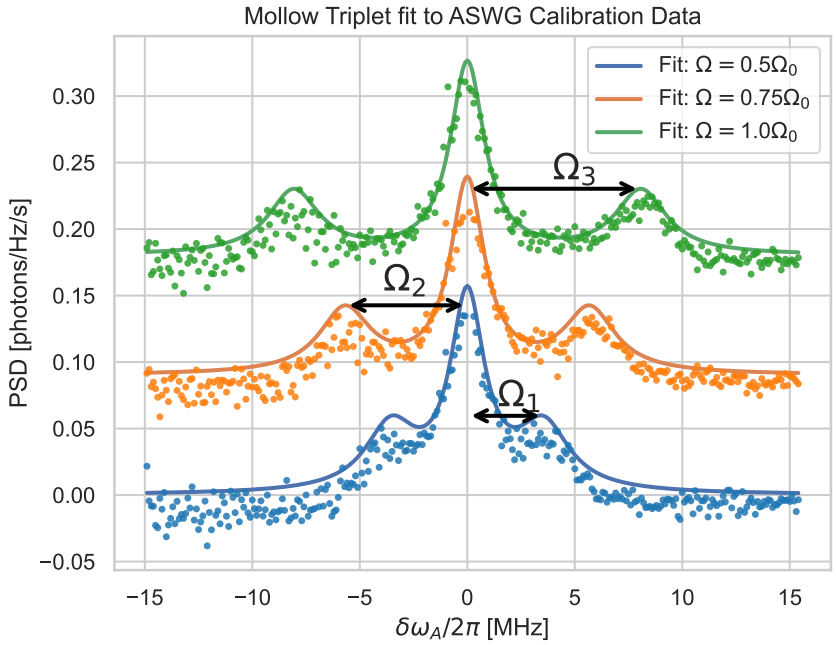

Figure 4.5: Mollow triplets fitted to the measured PSD from the ASWG while the $|0\rangle \rightarrow |A\rangle$ transition is driven at varying Rabi rates. The data and fits for $\Omega = 0.5\Omega_0, \Omega = 0.75\Omega_0$ have been offset in the y-axis for visibility.

To the fitted Rabi rates $(\Omega_1, \Omega_2, \Omega_3)$ a linear fit is performed of to the applied voltage, since the Rabi drive rate is proportional to the applied voltage: $\Omega \propto \sqrt{P} \rightarrow \Omega \propto V$. The result is shown in figure 4.6.

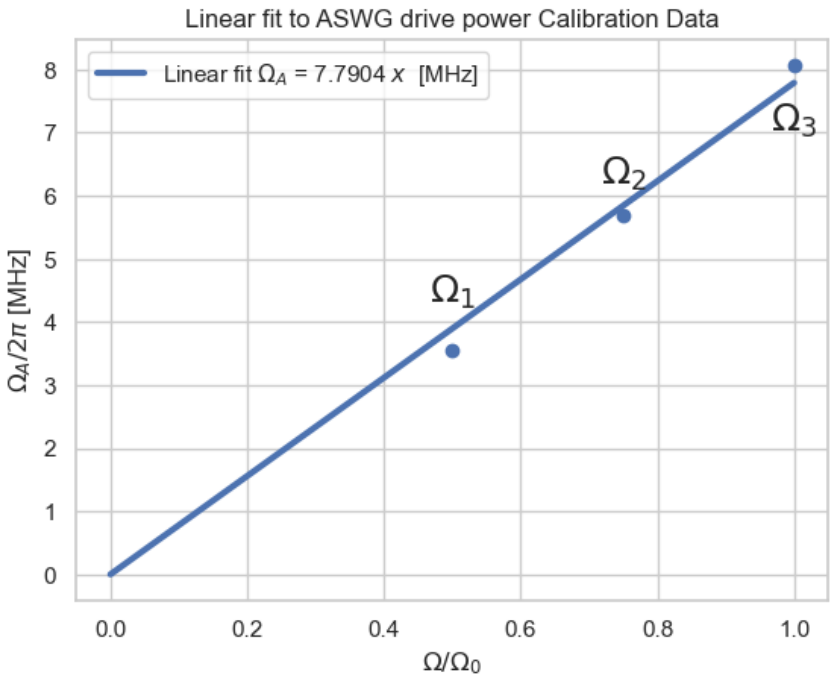

Figure 4.6: Linear fit to the different fitted Ω values for each pump power.

The fit is quite good and as expected we see that the Rabi rate follows a linear trend as a function of the applied voltage. The deviation from theory can probably be accounted to the SNR of the ASWG. To this end more averages could be performed for each point Ω, or more points Ω could be added to the measurement. Alternatively a different method of measuring the Rabi rate could be used. For example a reflection measurement as was used for the reflection spectroscopy, but with more averages performed to extract Ω more precisely.

4.2.2 Dephasing calibration

To find how strong the effect of the dephasing noise is a reflection measurement was performed while varying the power of the dephasing noise. The dephasing noise is sent in through one of the flux lines of the sample and couples to the system as described in 2.6.1. In figure 4.7 we can see the effect of the dephasing noise on the symmetric mode. The usually narrow minimum centered around ω_S is broadened with increasing dephasing noise indicating that the non-radiative decay rates are increased. The slight shift of the mode towards highers frequencies when more dephasing noise is sent to the system could be an effect of the AC Stark effect, but we are not certain about this. To draw any definite conclusions about this would require further studies into how the dephasing noise potentially shifts the mode frequencies.

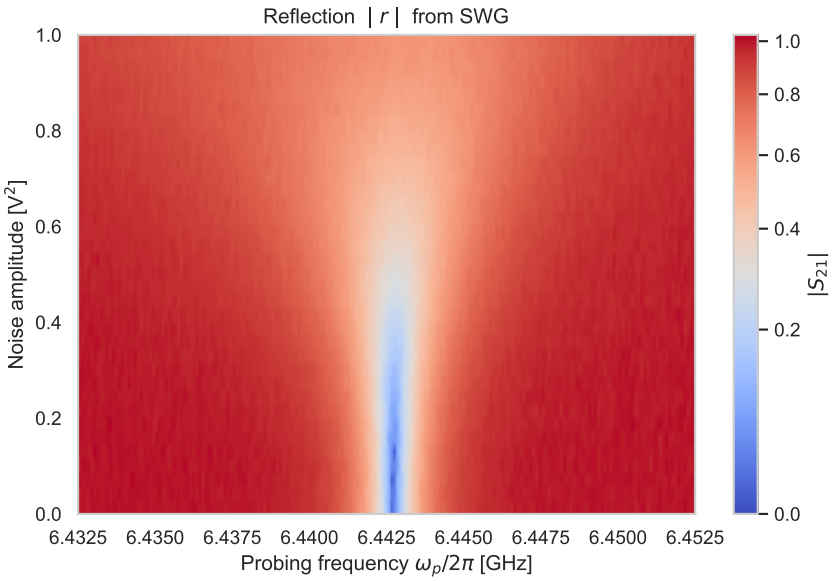

Figure 4.7: Reflection from the symmetric mode close to the magic power while sweeping power of the dephasing noise centered around $2g$.

To the acquired data equation 2.65 is fitted against the power [V^2] for each measured dephasing power where Γ_ϕ is the only fitting parameter as the two decay rates Γ_r, Γ_{nr} are known. We find a linear dependency of the dephasing to the noise power.

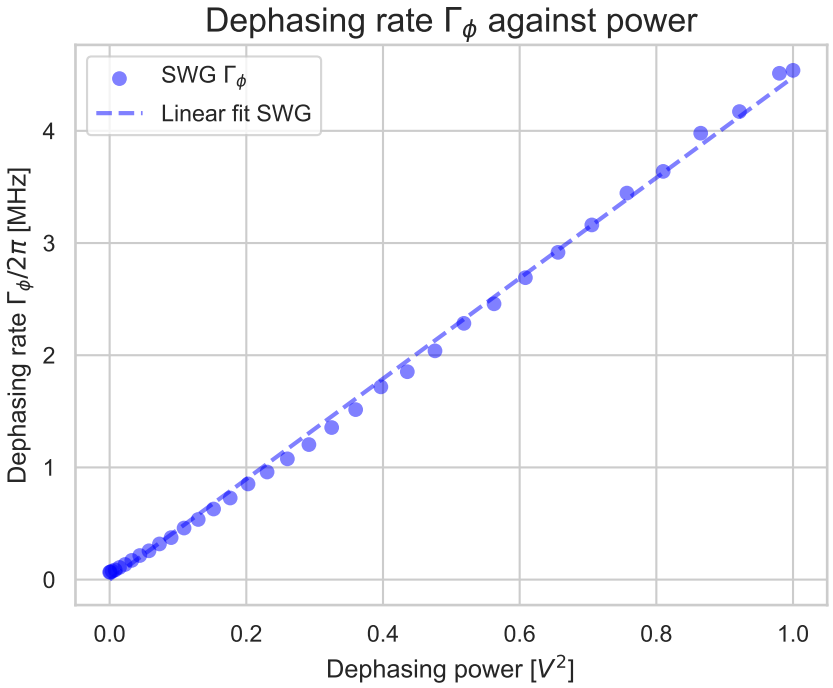

Figure 4.8: Dephasing noise and linear fit as a function of the applied power of the dephasing noise.

We see that the fitted dephasing noise of the SWG and ASWG match quite well but that the noise close to 0 applied dephasing deviates from the otherwise linear trend.

This could be due to the effect of the noise power being too small to observe in the reflection measurement used. The better fit to the SWG data is probably an effect of the TWPA installed on that line which increases the SNR.

4.2.3 Base temperature of the SWG

To find the an approximate temperature of the SWG the method described in section 2.4.2 is applied. The power is swept while the reflection is measured using a VNA.

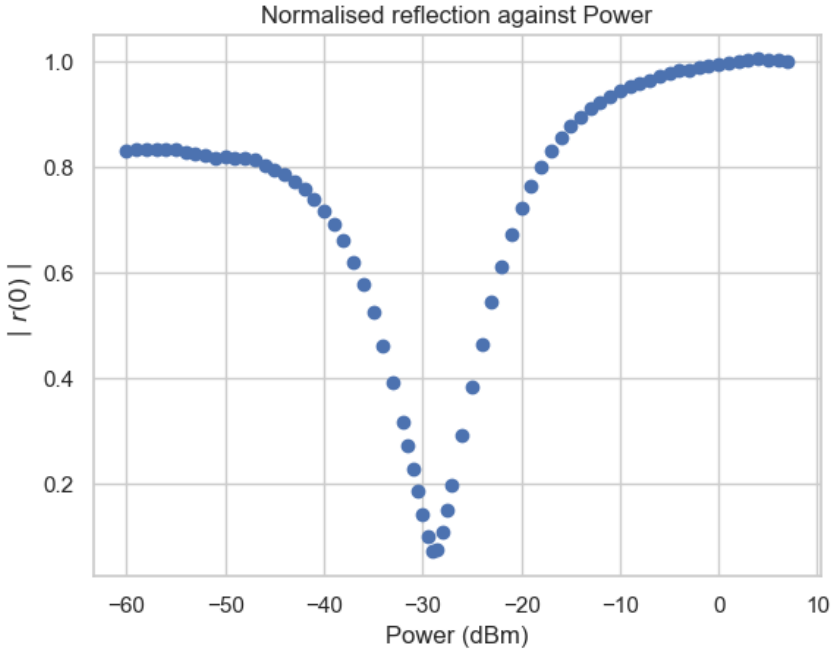

Figure 4.9: Reflection measurement of SWG against the probing power. The probing tone has frequency $\omega = \omega_S$.

To the data equation 2.66 is fitted for low powers to extract the temperature of the qubit. We find that the temperature is approximately $T_{qb} = 38$mK. This is added as a constant to the noise power of the background, whose measurements did not include this temperature as it is removed when subtracting the background of those PSD measurements.

4.3 PSD Power transfer

With the driving strength and dephasing noise calibrated we now measure the power transfer from the anti-symmetric mode to the symmetric mode by performing a PSD measurement at the SWG while coherently driving the $|0\rangle \rightarrow |A\rangle$ transition and applying dephasing noise driving the population transfer between $|A\rangle \leftrightarrow |S\rangle$. The first measurement was performed while varying the strength of the dephasing noise for a fixed driving strength Ω_A. The SWG is not populated with any thermal field so the temperature is approximately equal to 38mK. The raw data of the measured PSD is scaled by the factor extracted from the Mollow tripled fit on the SWG. To each

measured PSD a Gaussian is fitted to make the integrated currents less susceptible to outlier data points. A Gaussian fit is chosen as this was the functional form that best fits the data of the ones considered by comparison of the Residual Sum of Squares between the fits and data. For a more accurate the emission spectrum for this system would need to be calculated as was done for the Mollow triplet measurements, as described in section 2.3.2.

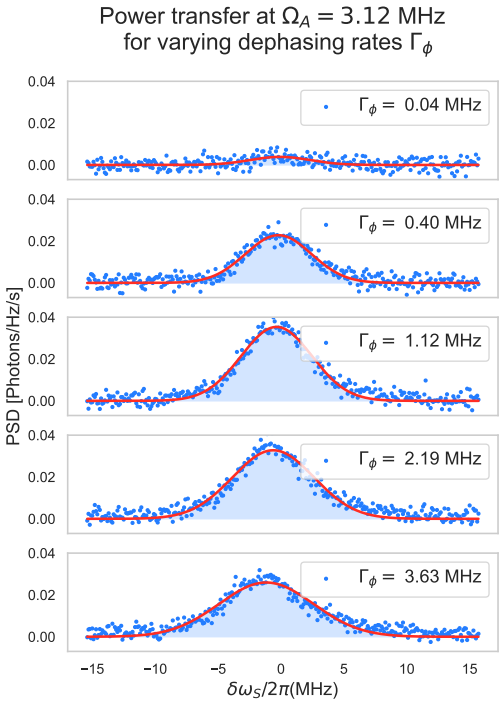

Figure 4.10: PSD measurements for varying strengths of the dephasing noise where a Gaussian (red) has been fitted to each data set. The area in shaded blue is the integrated current corresponding to J. For each plot 1 million averages have been computed.

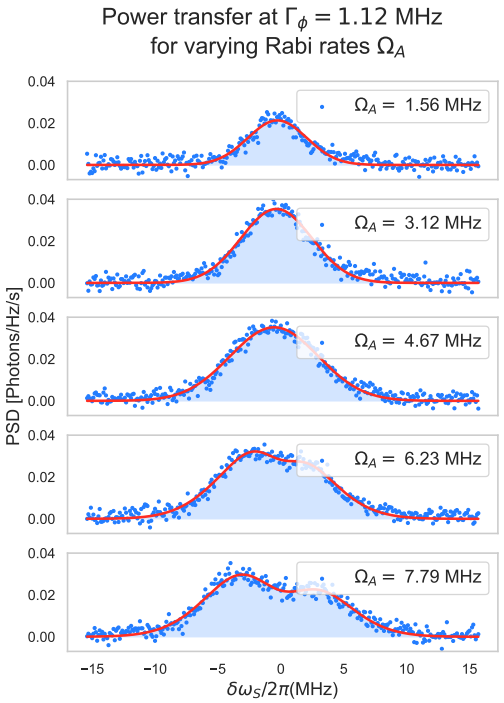

Figure 4.11: PSD measurements for varying pumping power where a Gaussian (red) has been fitted to each data set. The area in shaded blue is the integrated current corresponding to J. Each plot represents an average of 1 million computations.

In figure 4.10 we see the the power transfers dependency on the amplitude of the dephasing noise. We also note that at higher powers the emission spectrum i broadened. Next we perform the same PSD measurement for a fixed dephasing strength while varying the driving power Ω_A to see its effect on the power transfer, the result of which is shown in figure 4.11. As expected we see that as the pump is increased we see a larger power transfer taking place between the modes. We also note that at very high powers the emission spectrum is being split into two distinct modes as an effect of the strong pump. Indicating that the eigenmode at ω_S is being split into two separate states emitting photons to the SWG. To these data sets two Gaussian distributions are are fitted. The modes splitting at high driving rates will not be an issue for later measurements where the fluctuations are measured as those are performed at an intermediate driving strength.

4.4 Measuring heat current and its fluctuations

With a setup identical as when measuring the PSD of the power transfer we now measure the fluctuations in the current as described in section 2.8 and 3.4.2 utilizing Parsevals theorem. As the demodulation of the time trace will differ from that of the PSD measurements, one of the points of the time trace measurements is performed at with the exact same parameters for the Γ_ϕ, Ω_A and temperature T as one of the PSD measurements. This as a means of relating the time trace measurements to the Mollow triplet calibration previously performed and scale them to SI units. The integration time of the measurement is set to $\tau = 10\mu$s which is in agreement with being in the long time limit, as $T_1 = \frac{1}{\Gamma} = 0.0644\mu$s as assumed in section 2.8.

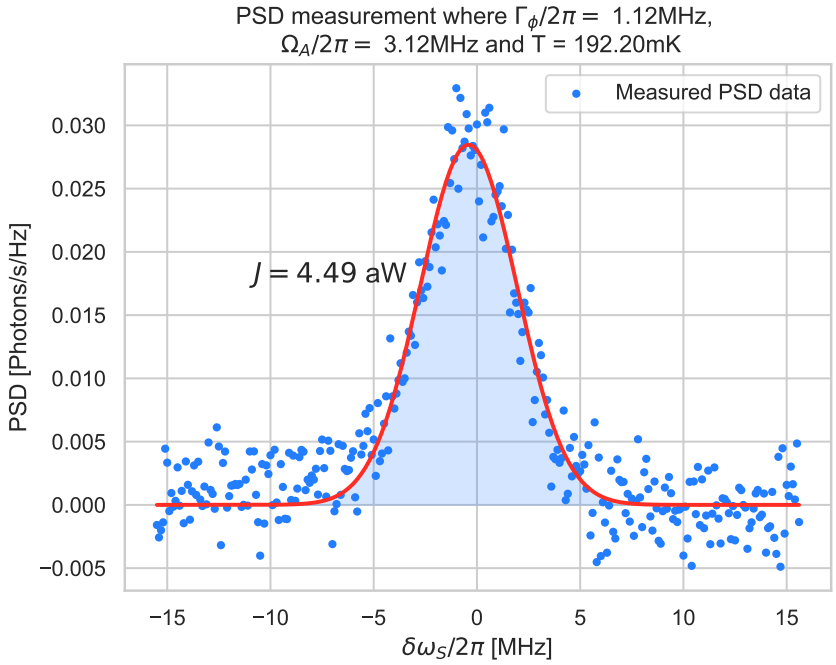

Figure 4.12: PSD measurement used to calibrate the time trace measurements. Shown in red is a Gaussian fit to the measurement data which is integrated to calculate the current J going into the SWG .

The time trace measurement was performed for the same fixed values of Γ_ϕ and Ω_A as the PSD measurement while varying the amplitude of the synthesised thermal field in the SWG. In addition to saving the integrated current $\langle Q_T \rangle$, the square of the signal, $\langle Q_T^2 \rangle$ is also computed and saved on the ADC. The measurement is performed 60 million times per point and the ensemble average saved is saved for the quantities $\langle Q_T \rangle_{\text{on}}, \langle Q_T^2 \rangle_{\text{on}}, \langle Q_T \rangle_{\text{off}}, \langle Q_T^2 \rangle_{\text{off}}$ as described in section 2.8. Q is the integrated current of the signal and the subscripts indicates if the dephasing noise is turned on mediating the population transfer or not. The measurement data is scaled to SI units by relating them to the PSD measurement in 4.12, call this calibration current $\phi_{\text{calibration}}$. The scaling by which the time trace measurements are multiplied

is

$$S = \frac{\phi_{\text{calibration}} T}{\langle Q_T \rangle_{\text{on}} - \langle Q_T \rangle_{\text{off}}}. \tag{4.1}$$

S relates the measured quantities to unitless quantities that can be added and subtracted as is needed. We are now ready to calculate the (unitless) current J, diffusion coefficient D and entropy production rate σ as

$$J = \left(\langle Q_T \rangle_{\text{on}} - \langle Q_T \rangle_{\text{off}} \right) S, \tag{4.2}$$

$$D = (\langle Q_T^2 \rangle_{\text{on}} - \langle Q_T \rangle_{\text{on}}^2) S^2 - (\langle Q_T^2 \rangle_{\text{off}} - \langle Q_T \rangle_{\text{off}}^2) S^2 - \frac{2-\eta}{\eta} J, \tag{4.3}$$

$$\sigma = \beta J \hbar \omega_s. \tag{4.4}$$

The measured integrated current in terms of number of photons and entropy production are shown in figure 4.13 and compared to what FCS theory predicts.

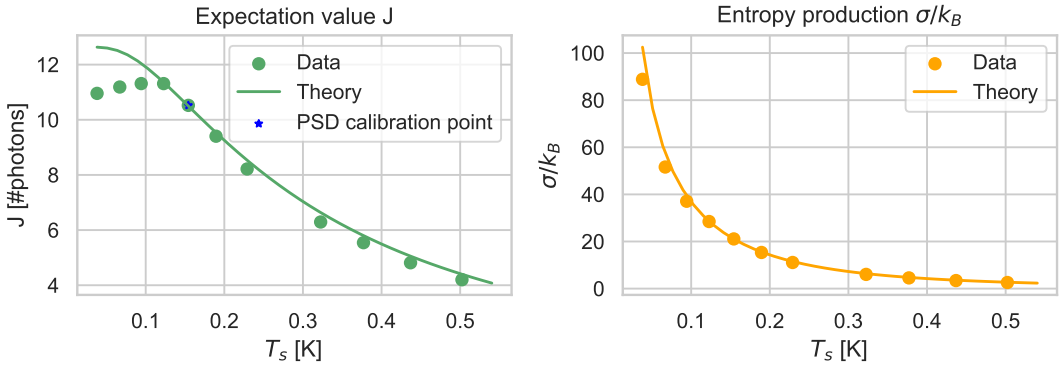

Figure 4.13: Experimentally measured photon current (left) and the associated entropy production (right) plotted against the temperature of the SWG, both compared against the theoretical predictions of each.

We see that the measured heat currents and entropy production follow the trends that theory predicts very well except for at temperatures very close to 0K. The fact that both the entropy and current match with theory is not surprising, since both are dependent on J, where the entropy is in essence just a scaling of the current with a factor $\frac{1}{T}$. But it does indicate a correctly measured temperature of the SWG. The visible trend is that the current decreases with temperature, possibly explained by more photons being absorbed by the system from the symmetric waveguide. No particular reason can be thought of that explains the slight deviation from theory at very low temperatures. We then calculate the variance in the photon currents to see how it compares to theory, shown in figure 4.14.

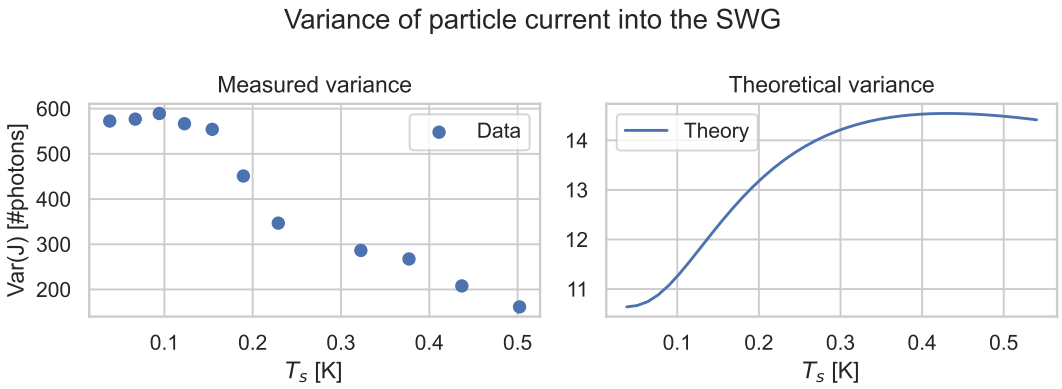

Figure 4.14: Experimentally measured variance (left) compared to what FCS theory predicts (right).

The difference between theory and the measured variance are significant. The two differ both in the range of values, and visible trends as functions of the temperature. With the theory predicting a higher variance with higher temperatures, whereas the measured variance decreases with temperature. The measured variance does not violate any known theory but seems to be an unlikely result as this would mean that the standard deviation (std $= \sqrt{\mathrm{Var}(J)}$) of the currents is much larger than the currents themselves. Due to the poor agreement between the simulations and experiment we are unable to draw any conclusions as to what the TUR ratio $\frac{\sigma}{k_b}\frac{\mathrm{Var}(J)}{J^2}$ associated with this thermal process is.

Some uncertainty between theory and measurement is to be expected from the extracted dephasing rate Γ_ϕ, driving strength Ω_A and the temperature of the SWG T_S. But the excellent agreement between simulations and the measured currents and entropy production indicate that these are not the leading cause of disagreement between theory and experiment. Another potential cause of error is the number of averages per point. Despite the 60 million averages taken per point the low SNR of the readout of SWG becomes even smaller when saving the squared second moment $\langle Q_T^2 \rangle$. For this reason more averages, or a better calibrated TWPA, would help in reducing the uncertainty of the measurement and potentially decrease the variation.

For further investigation of what causes the theory and experiment to disagree it would also be worthwhile to verify that the master equation used in simulations is correct. The lack of dissipators coupling the system to environment of the ASWG could potentially cause the deviation we see from theory. It would also be interesting to include higher excited energy states in the simulations to see if these make any significant changes to the results.

5
Discussion

In this project, we have implemented an experimental method for measuring currents and their fluctuations in quantum systems using superconducting qubits cooled to ultra-low temperatures. The results are promising for future measurements of current fluctuations in quantum systems, as there is good agreement between the measurements and theory when measuring the currents and entropy production in the system. However, the large deviations between theory and experiment in the fluctuation measurements indicate that there is much left to do to fully realize thermal advantages in quantum systems through TUR violations. We have identified several potential sources of error that could be causing the poor fit of the data to theory.

The isolation between the modes is not as high as previously demonstrated. In earlier studies, the sample used had an isolation close to 30 for each mode. The low isolation could potentially cause the emission from the symmetric mode to be emitted into the ASWG, which is not monitored, leading to larger variations in the measured currents.

There were clear indications of cross talk between the sample used and another mounted in the same tower in the cryostat through their flux lines. The exact effects of this are not known, but it could introduce dephasing noise to the system. This noise cannot be accounted for in the reflection fits performed when measuring the coupling rates of each mode. Especially this would make the calibration of the dephasing rate Γ_ϕ unreliable, as the assumption that $\Gamma_\phi = 0$ might not hold true when no dephasing noise is sent to the device. To verify if this is the case a PSD measurement where no dephasing noise is applied could be applied to see if any population transfer is taking place.

The theoretical background for measuring current fluctuations could also be revisited and compared to a measurement of the second order coherence function $g^{(2)}(\tau)$ to see how the two methods compare. A limiting factor of this would be the measurement time, since computing $g^{(2)}(\tau)$ is computationally heavy and requires significantly more averages than the performed PSD measurements. We could also verify the validity of the measurement technique by measuring the variance of a signal with a know probability distribution, such as a coherent tone or a true thermal field (one which is not synthesised using an AWG).

In conclusion, in this project, we have investigated the possibility of measuring current fluctuations in a circuit QED environment with the goal of showcasing thermal

advantages in quantum systems. A method for measuring fluctuations of photon currents is presented and experimentally implemented. In state-of-the-art measurements, heat currents of photons and their fluctuations are measured and compared to theory, where we find some agreement. The findings raise several intriguing questions that can help guide us toward the realization of quantum thermal machines that have precision advantages over classical systems.

5.1 Note added in proof

The issue related to measuring the variance of a photon current was resolved before the publication of this thesis. The observed deviation from theoretical predictions was caused by rounding errors in the DAC device, which significantly increased the variance, as shown in Figure 4.14. Specifically, the DAC rounded a large proportion of the measured values of $\langle Q_{on/off} \rangle^2$ and $\langle Q^2_{on/off} \rangle$ to zero because they fell below the device's numerical precision.

To address this, attenuation at the DAC input was removed, increasing the signal amplitude. Additionally, when necessary, the measured values were multiplied by a scaling factor to ensure that $\langle Q_{on/off} \rangle^2$ and $\langle Q^2_{on/off} \rangle$ remained within the computational range of the DAC. This effectively rescaled the scaling coefficient S in Equation 4.1.

These adjustments have enabled accurate measurements of the variance of photon currents, aligning them with theoretical expectations. Consequently, this has allowed for precise determination of the TUR ratio associated with the process.

Bibliography

[1] Richard P. Feynman. "Simulating physics with computers". In: *International Journal of Theoretical Physics* 21.6–7 (June 1982), pp. 467–488. ISSN: 1572-9575. DOI: 10.1007/bf02650179. URL: http://dx.doi.org/10.1007/BF02650179.

[2] Bruce W Shore and Peter L Knight. "The Jaynes-Cummings model". In: *J. Mod. Opt.* 40.7 (1993), pp. 1195–1238.

[3] Serge Haroche. "Nobel Lecture: Controlling photons in a box and exploring the quantum to classical boundary". In: *Rev. Mod. Phys.* 85 (3 2013), pp. 1083–1102. DOI: 10.1103/RevModPhys.85.1083. URL: https://link.aps.org/doi/10.1103/RevModPhys.85.1083.

[4] Andreas Bengtsson et al. "Improved Success Probability with Greater Circuit Depth for the Quantum Approximate Optimization Algorithm". In: *Phys. Rev. Appl.* 14 (3 2020), p. 034010. DOI: 10.1103/PhysRevApplied.14.034010. URL: https://link.aps.org/doi/10.1103/PhysRevApplied.14.034010.

[5] Mohammed Ali Aamir et al. *Thermally driven quantum refrigerator autonomously resets superconducting qubit*. 2023. arXiv: 2305.16710 [quant-ph]. URL: https://arxiv.org/abs/2305.16710.

[6] Alex Arash Sand Kalaee, Andreas Wacker, and Patrick P. Potts. "Violating the thermodynamic uncertainty relation in the three-level maser". In: *Physical Review E* 104.1 (July 2021). ISSN: 2470-0053. DOI: 10.1103/physreve.104.l012103. URL: http://dx.doi.org/10.1103/PhysRevE.104.L012103.

[7] Kacper Prech, Patrick P. Potts, and Gabriel T. Landi. *Role of Quantum Coherence in Kinetic Uncertainty Relations*. 2024. arXiv: 2407.14147 [quant-ph]. URL: https://arxiv.org/abs/2407.14147.

[8] J.R Waldram. *Superconductivity of Metals and Cuprates*. Ed. by J. R. Waldram. Dec. 2017. DOI: 10.1201/9780203737934. URL: http://dx.doi.org/10.1201/9780203737934.

[9] B.D. Josephson. "Possible new effects in superconductive tunnelling". In: *Physics Letters* 1.7 (July 1962), pp. 251–253. ISSN: 0031-9163. DOI: 10.1016/0031-9163(62)91369-0. URL: http://dx.doi.org/10.1016/0031-9163(62)91369-0.

[10] David J. Griffiths and Darrell F. Schroeter. *Introduction to Quantum Mechanics*. Cambridge University Press, Aug. 2018. ISBN: 9781107189638. DOI: 10.1017/9781316995433. URL: http://dx.doi.org/10.1017/9781316995433.

[11] J. J. Sakurai and Jim Napolitano. *Modern Quantum Mechanics*. Cambridge University Press. ISBN: 978-1108473224.

[12] G. Lindblad. "On the generators of quantum dynamical semigroups". In: *Communications in Mathematical Physics* 48.2 (June 1976), pp. 119–130. ISSN: 1432-0916. DOI: 10.1007/bf01608499. URL: http://dx.doi.org/10.1007/BF01608499.

[13] Johansson, G. *Open Quantum System Lecture Notes*. asb.sd. Accessed: 2024-04-23. 2023.

[14] Jens Koch et al. "Charge-insensitive qubit design derived from the Cooper pair box". In: *Physical Review A* 76.4 (Oct. 2007). ISSN: 1094-1622. DOI: 10.1103/physreva.76.042319. URL: http://dx.doi.org/10.1103/PhysRevA.76.042319.

[15] J. A. Schreier et al. "Suppressing charge noise decoherence in superconducting charge qubits". In: *Phys. Rev. B* 77 (18 2008), p. 180502. DOI: 10.1103/PhysRevB.77.180502. URL: https://link.aps.org/doi/10.1103/PhysRevB.77.180502.

[16] P. Krantz et al. "A quantum engineer's guide to superconducting qubits". In: *Applied Physics Reviews* 6.2 (June 2019). ISSN: 1931-9401. DOI: 10.1063/1.5089550. URL: http://dx.doi.org/10.1063/1.5089550.

[17] Emely Wiegand. "Quantum Optics and Waveguide Quantum Electrodynamics in Superconducting Circuits". PhD Dissertation. Göteborg, Sweden: Chalmers University of Technology, 2021. ISBN: 978-91-7905-477-9.

[18] Alexandre Blais et al. "Circuit quantum electrodynamics". In: *Reviews of Modern Physics* 93.2 (May 2021). ISSN: 1539-0756. DOI: 10.1103/revmodphys.93.025005. URL: http://dx.doi.org/10.1103/RevModPhys.93.025005.

[19] Christopher Gerry and Peter Knight. *Introductory Quantum Optics*. Cambridge, England: Cambridge University Press, Oct. 2004.

[20] Johansson, G. *From Quantum Optics to Quantum Technologies Lecture Notes*. https://chalmers.instructure.com/courses/25527/pages/lecture-notes-2023?module_item_id=381427. Accessed: 2024-06-30. 2023.

[21] Yong Lu et al. "Characterizing decoherence rates of a superconducting qubit by direct microwave scattering". In: *npj Quantum Information* 7.1 (Feb. 2021). ISSN: 2056-6387. DOI: 10.1038/s41534-021-00367-5. URL: http://dx.doi.org/10.1038/s41534-021-00367-5.

[22] Anton Frisk Kockum. "Quantum optics with artificial atoms". PhD Dissertation. Göteborg, Sweden: Chalmers University of Technology, 2014. ISBN: 978-91-7597-113-1.

[23] C. W. Gardiner and M. J. Collett. "Input and output in damped quantum systems: Quantum stochastic differential equations and the master equation". In: *Phys. Rev. A* 31 (6 1985), pp. 3761–3774. DOI: 10.1103/PhysRevA.31.3761. URL: https://link.aps.org/doi/10.1103/PhysRevA.31.3761.

[24] Marco Scigliuzzo et al. “Primary Thermometry of Propagating Microwaves in the Quantum Regime”. In: *Phys. Rev. X* 10 (4 2020), p. 041054. DOI: 10.1103/PhysRevX.10.041054. URL: https://link.aps.org/doi/10.1103/PhysRevX.10.041054.

[25] Frank P Incropera et al. *Fundamentals of heat and mass transfer*. en. 6th ed. Nashville, TN: John Wiley & Sons, Sept. 2006.

[26] Patrick P. Potts. *Quantum Thermodynamics*. 2024. arXiv: 2406.19206 [quant-ph]. URL: https://arxiv.org/abs/2406.19206.

[27] Gabriel T. Landi et al. “Current Fluctuations in Open Quantum Systems: Bridging the Gap Between Quantum Continuous Measurements and Full Counting Statistics”. In: *PRX Quantum* 5.2 (Apr. 2024). ISSN: 2691-3399. DOI: 10.1103/prxquantum.5.020201. URL: http://dx.doi.org/10.1103/PRXQuantum.5.020201.

[28] Jordan M. Horowitz and Todd R. Gingrich. “Thermodynamic uncertainty relations constrain non-equilibrium fluctuations”. In: *Nature Physics* 16.1 (Nov. 2019), pp. 15–20. ISSN: 1745-2481. DOI: 10.1038/s41567-019-0702-6. URL: http://dx.doi.org/10.1038/s41567-019-0702-6.

[29] Patrick P. Potts and Peter Samuelsson. “Thermodynamic uncertainty relations including measurement and feedback”. In: *Phys. Rev. E* 100 (5 2019), p. 052137. DOI: 10.1103/PhysRevE.100.052137. URL: https://link.aps.org/doi/10.1103/PhysRevE.100.052137.

[30] Simon Sundelin et al. *Quantum refrigeration powered by noise in a superconducting circuit*. 2024. arXiv: 2403.03373 [quant-ph]. URL: https://arxiv.org/abs/2403.03373.

[31] Wikipedia. *Dilution refrigerator — Wikipedia, The Free Encyclopedia*. http://en.wikipedia.org/w/index.php?title=Dilution%20refrigerator&oldid=1173661266. [Online; accessed 10-August-2024]. 2024.

[32] Mohammed Ali Aamir et al. “Engineering Symmetry-Selective Couplings of a Superconducting Artificial Molecule to Microwave Waveguides”. In: *Phys. Rev. Lett.* 129 (12 2022), p. 123604. DOI: 10.1103/PhysRevLett.129.123604. URL: https://link.aps.org/doi/10.1103/PhysRevLett.129.123604.

[33] Wikipedia. *Friis formulas for noise — Wikipedia, The Free Encyclopedia*. http://en.wikipedia.org/w/index.php?title=Friis%20formulas%20for%20noise&oldid=1187458365. [Online; accessed 13-August-2024]. 2024.

[34] George B Arfken, Hans J Weber, and Frank E Harris. “Mathematical Preliminaries”. In: *Mathematical Methods for Physicists*. Elsevier, 2013, pp. 1–82.

[35] Fei Yan et al. “Distinguishing Coherent and Thermal Photon Noise in a Circuit Quantum Electrodynamical System”. In: *Phys. Rev. Lett.* 120 (26 2018), p. 260504. DOI: 10.1103/PhysRevLett.120.260504. URL: https://link.aps.org/doi/10.1103/PhysRevLett.120.260504.

DEPARTMENT OF SOME SUBJECT OR TECHNOLOGY
CHALMERS UNIVERSITY OF TECHNOLOGY
Gothenburg, Sweden
www.chalmers.se

CHALMERS
UNIVERSITY OF TECHNOLOGY